Delft University of Technology

A Fixed-Wing UAV Formation Algorithm Based on Vector Field Guidance

Wang, Ximan; Baldi, Simone; Feng, Xuewei; Wu, Changwei; Xie, Hongwei; De Schutter, Bart

DOI
10.1109/TASE.2022.3144672

Publication date
2023

Document Version
Final published version

Published in
IEEE Transactions on Automation Science and Engineering

Citation (APA)
Wang, X., Baldi, S., Feng, X., Wu, C., Xie, H., & De Schutter, B. (2023). A Fixed-Wing UAV Formation Algorithm Based on Vector Field Guidance. *IEEE Transactions on Automation Science and Engineering*, *20*(1), 179-192. https://doi.org/10.1109/TASE.2022.3144672

Important note
To cite this publication, please use the final published version (if applicable).
Please check the document version above.

Copyright
Other than for strictly personal use, it is not permitted to download, forward or distribute the text or part of it, without the consent of the author(s) and/or copyright holder(s), unless the work is under an open content license such as Creative Commons.

Takedown policy
Please contact us and provide details if you believe this document breaches copyrights.
We will remove access to the work immediately and investigate your claim.

This work is downloaded from Delft University of Technology.
For technical reasons the number of authors shown on this cover page is limited to a maximum of 10.

Green Open Access added to TU Delft Institutional Repository

'You share, we take care!' - Taverne project

https://www.openaccess.nl/en/you-share-we-take-care

Otherwise as indicated in the copyright section: the publisher
is the copyright holder of this work and the author uses the
Dutch legislation to make this work public.

A Fixed-Wing UAV Formation Algorithm Based on Vector Field Guidance

Ximan Wang, Simone Baldi, *Senior Member, IEEE*, Xuewei Feng, Changwei Wu, Hongwei Xie, and Bart De Schutter, *Fellow, IEEE*

***Abstract*—The vector field method was originally proposed to guide a single fixed-wing Unmanned Aerial Vehicle (UAV) towards a desired path. In this work, a non-uniform vector field method is proposed that changes in both magnitude and direction, for the purpose of achieving formations of UAVs. As compared to related work in the literature, the proposed formation control law does not need to assume absence of wind. That is, due to the effect of the wind on the UAV, one can handle the UAV air speed being different from its ground speed, and the UAV heading angle being different from its course angle. Stability of the proposed formation method is analyzed via Lyapunov stability theory, and validations are carried out in software-in-the-loop and hardware-in-the-loop comparative experiments.**

***Note to Practitioners*—The software-in-the-loop and hardware-in-the-loop experiments, which are done with PX4 autopilot software and hardware, show that the proposed method can be implemented on board of UAVs and integrated with the control architecture of existing autopilot suites. Comparisons with standard formation algorithms show that the proposed method is effective in achieving formation in different path scenarios.**

***Index Terms*—Formation control, vector field, unmanned aerial vehicles, hardware-in-the-loop, PX4 autopilot.**

I. Introduction

FIXED-WING Unmanned Aerial Vehicles (UAVs) are becoming more and more popular for research and for applications in surveillance, search and rescue, photography, or entertainment [1]–[4]. Guidance algorithms are a crucial enabler to all these applications: the problem of UAV guidance has been examined in the literature from different points of view and recent surveys include [5]–[7]. Studies exist on exploiting communications or service-oriented characteristics of the surrounding environment to support UAV guidance tasks [8], [9]. However, despite the progress in the guidance for fixed-wing UAVs, up to now there are still limited or no established guidance tools for achieving formation tasks. To support this observation, notice that despite the several commercial or open-source autopilot suites developed for single UAVs (ArduPilot, PX4, DJI, NAVIO2, AscTec Trinity, etc.) none of them yet provides formation control functionalities. For a single fixed-wing UAV, the vector field method, formulated originally in [10], has become a well-established method for guidance towards a desired path. The vector field idea is based on generating a field of desired course inputs that become the reference input to the inner-loop attitude control laws. Extensions to the vector field idea include tracking targets [11], tracking general curved paths [12], tackling unmodeled course angle dynamics [13], or removing singularities in the vector field that prevent to achieve global convergence [14].

Motivated by these and other advances, the vector field method has gained popularity and studies have been made to extend it towards formation tasks: examples include circular formations with constant speed [15] or, when the velocity can be controlled, a non-uniform vector field whose vectors have different directions and magnitudes [16]. In this sense, the vector field method offers an alternative to formation-keeping methods based on PID control [17], inverse optimal control [18], Nash equilibrium [19], [20], model predictive control [21], [22], or consensus-based formation control [23]–[26]. It is worth mentioning that, while the vector field method has been originally developed for fixed-wing UAVs [27], not all the alternative methods are directly applicable to fixed-wing UAVs: consensus- and Nash equilibrium-based methods have been studied mostly for quadrotors [28] or for vertical takeoff and landing UAVs [29]; methods based on inverse optimal control or model predictive control require a different architecture than the established open-source architectures of many autopilot suites (e.g. ArduPilot, PX4, NAVIO2).

Vector-field-based formation control offers the appealing possibility of being integrated with autopilot suites for fixed-wing UAVs, which may be not straightforward with other approaches. For example, formation control laws based on the consensus approach are designed to deliver forces and torques (to affect velocities and angular rates). This is due

Manuscript received 2 December 2021; accepted 17 January 2022. Date of publication 8 February 2022; date of current version 6 January 2023. This article was recommended for publication by Associate Editor A. Pietrabissa and Editor C. Seatzu upon evaluation of the reviewers' comments. This work was supported in part by the Natural Science Foundation of China under Grant 62073074, in part by the Double Innovation Plan under Grant 4207012004, and in part by the Special Funding for Overseas under Grant 6207011901. *(Ximan Wang and Simone Baldi contributed equally to this work.) (Corresponding author: Simone Baldi.)*

Ximan Wang and Bart De Schutter are with the Delft Center for Systems and Control, TU Delft, 2628 Delft, The Netherlands (e-mail: x.wang-15@tudelft.nl; b.deschutter@tudelft.nl).

Simone Baldi is with the School of Cyber Science and Engineering and the School of Mathematics, Southeast University, Nanjing 211189, China, and also with the Delft Center for Systems and Control, TU Delft, 2628 Delft, The Netherlands (e-mail: s.baldi@tudelft.nl).

Xuewei Feng, Changwei Wu, and Hongwei Xie are with the College of Software, Taiyuan University of Technology, Taiyuan 030024, China (e-mail: fengxuewei0941@linktyut.edu.cn; wuchangwei1055@linktyut.edu.cn; xiehongwei@tyut.edu.cn).

Color versions of one or more figures in this article are available at https://doi.org/10.1109/TASE.2022.3144672.

Digital Object Identifier 10.1109/TASE.2022.3144672

1545-5955 © 2022 IEEE. Personal use is permitted, but republication/redistribution requires IEEE permission.
See https://www.ieee.org/publications/rights/index.html for more information.

Authorized licensed use limited to: TU Delft Library. Downloaded on January 20,2023 at 15:03:44 UTC from IEEE Xplore. Restrictions apply.

to the fact that the dynamics of the UAV are derived from Newton's law as double integrators or similar dynamics (this approach is used for quadrotors [30]–[32] and sometimes also for fixed-wing UAVs [33]). However, the typical control architecture of most of the aforementioned autopilot software suites is the successive loop closure, where inner loops are used to provide thrust and actuator deflections, while the guidance law (outer loop) is in charge of providing desired the velocity and the desired course [34], [35]. In some cases, the guidance law provides the velocity and the angular rate [36].

The approach that we take in this work is to consider that the autopilot is synthesized according to the successive loop closure architecture: this is in line with standard literature [37], [38] and standard books [34]. We propose a non-uniform vector field that changes in both magnitude and direction: the main contributions as compared to related work are:

- Recent literature has proposed the use of backstepping control to implement the vector field for formation tasks [37], [38]: however, with this method an assumption on the absence of wind is required (see next item). In this work, in place of backstepping, we adopt a philosophy that is closer to the originally proposed vector field approach, which relies on a sliding mode control method;
- In related literature, the absence of wind was assumed so that the UAV ground speed coincides with its air speed and the UAV course angle coincides with its heading angle. This setting is restrictive and does not hold in practice. By adopting a philosophy closer to the originally proposed vector field approach, we do not require zero wind: sliding-mode-based control commands are designed under the scenario that the air speed can be different from ground speed, and the heading angle can be different from the course angle.
- Besides analyzing stability of the proposed method, comparative experiments are provided in both software-in-the-loop and hardware-in-the-loop environments, using PX4 as software and hardware.

Comparisons with standard formation algorithms show that the proposed formation method is effective in in different path scenarios, even with high-latency communication (2Hz).

The rest of the paper is organized as follows: in Sect. II the vector field method for a single fixed-wing UAV is recalled. In Sect. III we provide the formation problem description and its solution. Software-in-the-loop and hardware-in-the-loop experiments are in Sect. IV: the method is implemented using PX4 as autopilot suite. Conclusions are Sect. V. Stability analysis is provided in the appendix by making use of Lyapunov theory.

II. Preliminaries on Vector Field

The vector field describes a field guiding towards desired locations. Traditionally, the vector field was proposed to follow line or orbit paths (cf. Figure 1a), but this idea can be extended to navigate through obstacles or perform more complex tasks. We will use the subscript "l" to indicate that the vector field is applied to the leader UAV, using the dynamics

$$\begin{aligned}\dot{x}_l &= V_{al}\cos(\psi_l) + W\cos(\psi_W) = V_{gl}\cos(\chi_l)\\ \dot{y}_l &= V_{al}\sin(\psi_l) + W\sin(\psi_W) = V_{gl}\sin(\chi_l)\\ \dot{\chi}_l &= \alpha_l(\chi_l^c - \chi_l).\end{aligned} \tag{1}$$

where ψ_l is the heading angle between the north and the air speed velocity V_{al}; x_l and y_l are the coordinates of the UAV in the inertial frame; W and ψ_W are the wind speed and wind angle; χ_l is the course and V_{gl} is the ground velocity, both resulting from the vector summation of air speed and wind, cf. the wind triangle in Figure 1b. In the last equation, χ_l^c is the command course (to be designed), and α_l is a positive constant that defines the inverse of the time constant of the course-hold loop. The interested reader is referred to standard literature [5], [27], [34], [39], [40] describing how dynamics (1) can be obtained for guidance purposes.

For a vector field described by a function $\chi_l^d(e_l)$, where e_l is the cross-track error, the guidance law takes the form

$$\chi_l^c = \chi_l - \frac{\dot{\chi}_l^d}{\alpha_l} - \frac{\kappa}{\alpha_l}\,\text{sat}\left(\frac{\tilde{\chi}_l}{\varepsilon}\right) \tag{2}$$

where $\tilde{\chi}_l = \chi_l - \chi_l^d$ is the course error with respect to the desired vector field, κ and ε are parameters governing control aggressiveness and boundary layer, and

$$\text{sat}(x) = \begin{cases} x & \text{if } |x| < 1,\\ \text{sgn}(x) & \text{otherwise.}\end{cases} \tag{3}$$

To clarify (2), let us consider the standard examples in Figure 1a. For a straight line vector field we have

$$\chi_l^d(e_l) = -\chi_\infty \frac{2}{\pi}\tan^{-1}(ke_l) \tag{4}$$

$$\chi_l^c = \chi_l - \frac{\chi_\infty}{\alpha_l}\frac{2}{\pi}\frac{kV_{gl}}{1+(ke_l)^2}\sin(\chi_l) - \frac{\kappa}{\alpha_l}\,\text{sat}\left(\frac{\tilde{\chi}_l}{\varepsilon}\right) \tag{5}$$

where e_l denotes the cross-track error with respect to the desired line (sometimes the notation e_y is used to indicate this error [27]), $\chi_\infty \in (0, \frac{\pi}{2}]$ is the course reference when the error is large, and k governs the vector field smoothness.

For another standard scenario, an orbit vector field, we have

$$\chi_l^d(e_l) = \gamma + \lambda\left(\frac{\pi}{2} + \tan^{-1}(ke_l)\right) \tag{6}$$

$$\begin{aligned}\chi_l^c = \chi_l &+ \frac{V_{gl}}{\alpha_l d}\sin(\chi_l - \gamma)\\ &+ \frac{V_{gl}}{\alpha_l}\frac{k}{1+(ke_l)^2}\cos(\chi_l - \gamma) - \frac{\kappa}{\alpha_l}\,\text{sat}\left(\frac{\tilde{\chi}_l}{\varepsilon}\right)\end{aligned} \tag{7}$$

where e_l denotes the cross-track error with respect to the desired orbit (sometimes the notation $\tilde{d} = d - R$ is used to indicate this error, where d is the distance of the UAV from the orbit center, R is the desired orbit radius [27]), R is the orbit radius, and γ is the angle between the north and the UAV position with respect to the orbit center. The parameters k, κ, ε have similar meanings as in the straight-line case.

III. Vector Field for Formation Control

This section explains how the vector field can be used to solve the formation control problem. To this purpose, consider the scenario in Figure 2 with a leader and a follower UAV (indexed with subscripts "l" and "f"). Their positions in the inertial frame are (x_l, y_l) and (x_f, y_f). The vectors V_{gl} and V_{gf}

Authorized licensed use limited to: TU Delft Library. Downloaded on January 20,2023 at 15:03:44 UTC from IEEE Xplore. Restrictions apply.

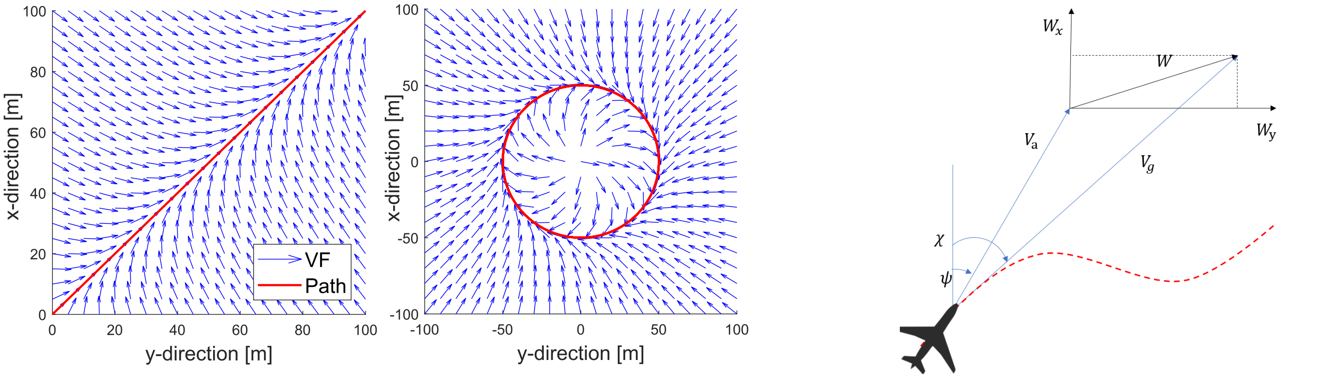

(a) Vector fields for straight line and orbit paths.

(b) Wind triangle, vector sum between air speed and wind.

Fig. 1. Preliminary concepts for the vector field method.

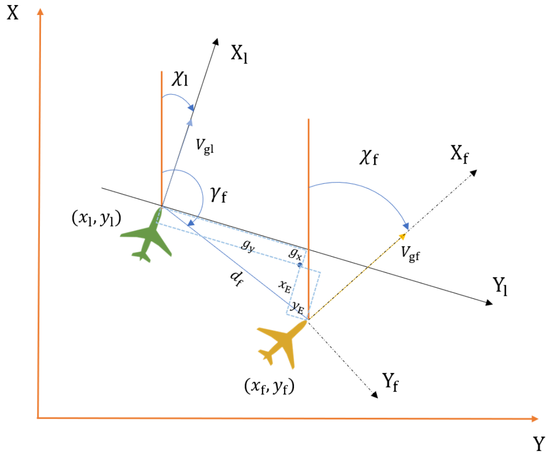

Fig. 2. Coordinates for formation error.

TABLE I
NOTATION

Symbol	Description	Unit
$(x_\mathrm{l}, y_\mathrm{l})$ $(x_\mathrm{f}, y_\mathrm{f})$	Coordinates of UAV_l and UAV_l in inertial frame	m
V_gl, V_gf	Ground speed	m/s
χ_l, χ_f	Course angle	rad
V_gl^d, V_gf^d	Desired speed	m/s
$\chi_\mathrm{l}^\mathrm{d}$, $\chi_\mathrm{f}^\mathrm{d}$	Desired course angle	rad
V_gl^c, V_gf^c	Speed command	m/s
χ_l^c, χ_f^c	Course angle command	rad
α_l, α_f	Inverse time constant of course-hold loop	s^{-1}
β_l, β_f	Inverse time constant of velocity-hold loop	s^{-1}
(g_x, g_y)	Desired gap in leader's body frame	m
d_f	Distance of UAV_f from UAV_l	m
γ_f	Angle between North and UAV_f with respect to leader position	rad
$(x_\mathrm{E}, y_\mathrm{E})$	Formation error in leader's body frame	m

are their ground speeds. Note from Figure 2 that the position to be tracked by the follower UAV is shifted by a vector that represents the desired formation gap. We refer to Table I for a list of symbols used in this work.

The dynamics of the leader are represented as in (1), with $\chi_\mathrm{l}^\mathrm{c}$ resulting from the standard vector field. Accordingly, the dynamics of the follower UAV are

$$\begin{aligned}\dot{x}_\mathrm{f} &= V_\mathrm{gf}\cos(\chi_\mathrm{f})\\ \dot{y}_\mathrm{f} &= V_\mathrm{gf}\sin(\chi_\mathrm{f})\\ \dot{\chi}_\mathrm{f} &= \alpha_\mathrm{f}(\chi_\mathrm{f}^\mathrm{c} - \chi_f)\\ \dot{V}_\mathrm{gf} &= \beta_\mathrm{f}(V_\mathrm{gf}^\mathrm{c} - V_\mathrm{gf}).\end{aligned} \tag{8}$$

The main difference between (8) and (1) is given by the last equation, which represents a velocity-hold loop, where β_f is the inverse of the time constant of the velocity-hold loop, and V_gf^c the speed command. In other words, we allow the follower to change its velocity V_gf in such a way as to achieve the formation. In several open-source autopilot suites (e.g. ArduPilot, PX4, NAVIO2) commanding the velocity is possible thanks to the Total Energy Control System (TECS), which controls velocity and altitude. The interested reader is again referred to standard literature [5], [27], [34], [39], [40] describing how dynamics (8) can be obtained.

In place of defining the formation error in the inertial frame, it is more convenient to express it in the leader's frame. Therefore, let (g_x, g_y) be the desired formation gap expressed in the leader's frame. In other words, the leader's frame represents the reference frame for the follower, which calculates the formation error in this frame as:

$$\begin{aligned}x_\mathrm{E} &= g_x + d_f\sin(\gamma_\mathrm{f} - \frac{\pi}{2} - \chi_\mathrm{l})\\ y_\mathrm{E} &= g_y + d_f\cos(\gamma_\mathrm{f} - \frac{\pi}{2} - \chi_\mathrm{l})\end{aligned} \tag{9}$$

where d_f is the distance of the follower UAV from the leader UAV, and γ_f is the angle between the north and the follower UAV position with respect to the leader position. The formation control problem can be formulated as:

Authorized licensed use limited to: TU Delft Library. Downloaded on January 20,2023 at 15:03:44 UTC from IEEE Xplore. Restrictions apply.

Control Problem: Given the leader dynamics (1) and the follower dynamics (8), design the follower commands $\chi_{\mathrm{f}}^{\mathrm{c}}$, $V_{\mathrm{gf}}^{\mathrm{c}}$ such that the errors x_{E}, y_{E}, $\chi_{\mathrm{f}} - \chi_{\mathrm{f}}^{\mathrm{d}}$ and $V_{\mathrm{gf}} - V_{\mathrm{gf}}^{d}$ converge to zero asymptotically. Here, $\chi_{\mathrm{f}}^{\mathrm{d}}$, and $V_{\mathrm{gf}}^{\mathrm{d}}$ are vector fields to be designed appropriately.

A. Error Dynamics

We first need to derive the error dynamics of the leader-follower system. These dynamics are useful to prove stability of the proposed approach. To describe the position of the follower with respect to the leader we use

$$\begin{aligned} x_{\mathrm{f}} &= x_{\mathrm{l}} + d_{\mathrm{f}} \cos(\gamma_{\mathrm{f}}) \\ y_{\mathrm{f}} &= y_{\mathrm{l}} + d_{\mathrm{f}} \sin(\gamma_{\mathrm{f}}) \end{aligned} \tag{10}$$

where d_{f} is the distance of the follower UAV from the leader UAV, and γ_{f} is the angle between the north and the follower UAV position with respect to the leader position.

We can now obtain the dynamics for γ_{f} and d_{f} in these coordinates by taking the derivative of (10) and using the dynamics of the follower in (8):

$$\begin{aligned} V_{\mathrm{gf}} \cos(\chi_{\mathrm{f}}) &= \dot{x}_{\mathrm{l}} + \dot{d}_{\mathrm{f}} \cos(\gamma_{\mathrm{f}}) - d_{\mathrm{f}} \sin(\gamma_{\mathrm{f}}) \dot{\gamma}_{\mathrm{f}} \\ V_{\mathrm{gf}} \sin(\chi_{\mathrm{f}}) &= \dot{y}_{\mathrm{l}} + \dot{d}_{\mathrm{f}} \sin(\gamma_{\mathrm{f}}) + d_{\mathrm{f}} \cos(\gamma_{\mathrm{f}}) \dot{\gamma}_{\mathrm{f}}. \end{aligned} \tag{11}$$

To obtain the dynamics $\dot{d}_{\mathrm{f}}$, we multiply the first equation in (11) by $\cos(\gamma_{\mathrm{f}})$ and the second equation by $\sin(\gamma_{\mathrm{f}})$. Next, we sum the two resulting equations:

$$\begin{aligned} V_{\mathrm{gf}} \cos(\chi_{\mathrm{f}} - \gamma_{\mathrm{f}}) &= \dot{x}_{\mathrm{l}} \cos(\gamma_{\mathrm{f}}) + \dot{y}_{\mathrm{l}} \sin(\gamma_{\mathrm{f}}) + \dot{d}_{\mathrm{f}} \\ \dot{d}_{\mathrm{f}} &= V_{\mathrm{gf}} \cos(\chi_{\mathrm{f}} - \gamma_{\mathrm{f}}) - \dot{x}_{\mathrm{l}} \cos(\gamma_{\mathrm{f}}) \\ &\quad - \dot{y}_{\mathrm{l}} \sin(\gamma_{\mathrm{f}}). \end{aligned} \tag{12}$$

Substituting $\dot{x}_{\mathrm{l}}$ and $\dot{y}_{\mathrm{l}}$ in (12) with the leader dynamics (1) gives:

$$\begin{aligned} \dot{d}_{\mathrm{f}} &= V_{\mathrm{gf}} \cos(\chi_{\mathrm{f}} - \gamma_{\mathrm{f}}) - V_{\mathrm{gl}} \cos(\chi_{\mathrm{l}}) \cos(\gamma_{\mathrm{f}}) \\ &\quad - V_{\mathrm{gl}} \sin(\chi_{\mathrm{l}}) \sin(\gamma_{\mathrm{f}}) \\ &= V_{\mathrm{gf}} \cos(\chi_{\mathrm{f}} - \gamma_{\mathrm{f}}) - V_{\mathrm{gl}} \cos(\chi_{\mathrm{l}} - \gamma_{\mathrm{f}}). \end{aligned} \tag{13}$$

In order to obtain $\dot{\gamma}_{\mathrm{f}}$ we take (11) and multiply the first equation by $\sin(\gamma_{\mathrm{f}})$ and the second equation by $\cos(\gamma_{\mathrm{f}})$. Then, we subtract the first from the second so as to obtain

$$\begin{aligned} V_{\mathrm{gf}} \sin(\chi_{\mathrm{f}} - \gamma_{\mathrm{f}}) &= -\dot{x}_{\mathrm{l}} \sin(\gamma_{\mathrm{f}}) + \dot{y}_{\mathrm{l}} \cos(\gamma_{\mathrm{f}}) + d_{\mathrm{f}} \dot{\gamma}_{\mathrm{f}} \\ \dot{\gamma}_{\mathrm{f}} &= \frac{V_{\mathrm{gf}}}{d_{\mathrm{f}}} \sin(\chi_{\mathrm{f}} - \gamma_{\mathrm{f}}) + \frac{\dot{x}_{\mathrm{l}}}{d_{\mathrm{f}}} \sin(\gamma_{\mathrm{f}}) \\ &\quad - \frac{\dot{y}_{\mathrm{l}}}{d_{\mathrm{f}}} \cos(\gamma_{\mathrm{f}}) \\ &= \frac{V_{\mathrm{gf}}}{d_{\mathrm{f}}} \sin(\chi_{\mathrm{f}} - \gamma_{\mathrm{f}}) - \frac{V_{\mathrm{gl}}}{d_{\mathrm{f}}} \sin(\chi_{\mathrm{l}} - \gamma_{\mathrm{f}}). \end{aligned} \tag{14}$$

Using (9) we finally derive the error dynamics

$$\begin{aligned} \dot{x}_{\mathrm{E}} &= \dot{d}_{\mathrm{f}} \sin(\gamma_{\mathrm{f}} - \frac{\pi}{2} - \chi_{\mathrm{l}}) + d_{\mathrm{f}} \cos(\gamma_{\mathrm{f}} - \frac{\pi}{2} - \chi_{\mathrm{l}}) \dot{\gamma}_{\mathrm{f}} \\ &= V_{\mathrm{gf}} \sin(\chi_{\mathrm{f}} - \frac{\pi}{2} - \chi_{\mathrm{l}}) + V_{\mathrm{gl}} \\ \dot{y}_{\mathrm{E}} &= \dot{d}_{\mathrm{f}} \cos(\gamma_{\mathrm{f}} - \frac{\pi}{2} - \chi_{\mathrm{l}}) - d_{\mathrm{f}} \sin(\gamma_{\mathrm{f}} - \frac{\pi}{2} - \chi_{\mathrm{l}}) \\ &= V_{\mathrm{gf}} \cos(\chi_{\mathrm{f}} - \frac{\pi}{2} - \chi_{\mathrm{l}}). \end{aligned} \tag{15}$$

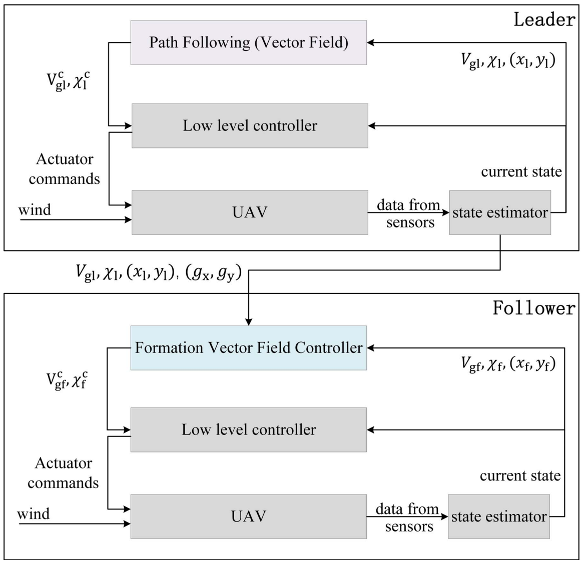
Leader
Path Following (Vector Field)
$V_{\mathrm{gl}}, \chi_{\mathrm{l}}, (x_{\mathrm{l}}, y_{\mathrm{l}})$
$V_{\mathrm{gl}}^{\mathrm{c}}, \chi_{\mathrm{l}}^{\mathrm{c}}$
Low level controller
Actuator commands
current state
wind
UAV
data from sensors
state estimator
$V_{\mathrm{gl}}, \chi_{\mathrm{l}}, (x_{\mathrm{l}}, y_{\mathrm{l}}), (g_{\mathrm{x}}, g_{\mathrm{y}})$
Follower
Formation Vector Field Controller
$V_{\mathrm{gf}}, \chi_{\mathrm{f}}, (x_{\mathrm{f}}, y_{\mathrm{f}})$
$V_{\mathrm{gf}}^{\mathrm{c}}, \chi_{\mathrm{f}}^{\mathrm{c}}$
Low level controller
Actuator commands
current state
wind
UAV
data from sensors
state estimator

Fig. 3. The flowchart of the algorithm.

Algorithm 1 Vector-Field-Based Formation Control

```
Input: $V_{\mathrm{gf}}, V_{\mathrm{gl}}, \chi_{\mathrm{f}}, \chi_{\mathrm{l}}, (g_x, g_y), (x_{\mathrm{l}}, y_{\mathrm{l}}), (x_{\mathrm{f}}, y_{\mathrm{f}})$
$\gamma_{\mathrm{f}} \leftarrow \mathrm{atan}((x_{\mathrm{f}}, y_{\mathrm{f}}) - (x_{\mathrm{l}}, y_{\mathrm{l}}))$
$d_{\mathrm{f}} \leftarrow ||((x_{\mathrm{f}}, y_{\mathrm{f}}) - (x_{\mathrm{l}}, y_{\mathrm{l}}))||$
$x_{\mathrm{E}} \leftarrow g_x + d_f \sin(\gamma_{\mathrm{f}} - \frac{\pi}{2} - \chi_{\mathrm{l}})$
$y_{\mathrm{E}} \leftarrow g_y + d_f \cos(\gamma_{\mathrm{f}} - \frac{\pi}{2} - \chi_{\mathrm{l}})$
$\chi_{\mathrm{f}}^{\mathrm{d}} \leftarrow \chi_{\mathrm{l}} + \chi_{\infty} \frac{2}{\pi} \tan^{-1}(k_y y_{\mathrm{E}})$, follower's desired course
$V_{\mathrm{gf}}^{\mathrm{d}} \leftarrow V_{\mathrm{gl}} + V_{\infty} \frac{2}{\pi} \tan^{-1}(k_x x_{\mathrm{E}})$, follower's desired ground speed
$\chi_{\mathrm{f}}^{c} \leftarrow \chi_{\mathrm{f}} + \frac{1}{\alpha} \dot{\chi}_{\mathrm{f}}^{d} - \frac{\kappa}{\alpha} \mathrm{sat}\big(\frac{\tilde{\chi}_{\mathrm{f}}}{\epsilon}\big)$, where $\tilde{\chi}_{\mathrm{f}} \leftarrow \chi_{\mathrm{f}} - \chi_{\mathrm{f}}^{\mathrm{d}}$
$V_{\mathrm{gf}}^{c} \leftarrow V_{\mathrm{gf}} + \frac{1}{\beta} \dot{V}_{\mathrm{gf}}^{d} + \frac{1}{\rho\beta} x_{\mathrm{E}} - \frac{\kappa}{\beta} \mathrm{sat}\Big(\frac{\tilde{V}_{\mathrm{gf}}}{\epsilon}\Big)$, where $\tilde{V}_{\mathrm{gf}} \leftarrow V_{\mathrm{gf}} - V_{\mathrm{gf}}^{d}$
Output: $\chi_{\mathrm{f}}^{c}, V_{\mathrm{gf}}^{c}$
```

The error dynamics depend on the difference between the course of the leader and the follower, the ground speed of the follower, and the ground speed of the leader, as one could intuitively expect. An alternative way to arrive at (15) is by using polar coordinates: however, this would require to introduce extra notation that might decrease readability. The error dynamics (15) will play a role in analyzing the stability of the formation control law.

B. Guidance Law for Follower

The vector field for the follower is defined in the leader frame and can be written as follows

$$\chi_{\mathrm{f}}^{\mathrm{d}} = \chi_{\mathrm{l}} + \chi_{\infty} \frac{2}{\pi} \tan^{-1}(k_y y_{\mathrm{E}}) \tag{16}$$

$$V_{\mathrm{gf}}^{\mathrm{d}} = V_{\mathrm{gl}} + V_{\infty} \frac{2}{\pi} \tan^{-1}(k_x x_{\mathrm{E}}) \tag{17}$$

where V_{∞} is the maximum ground speed correction of the follower when the tracking error is very large (the maximum ground speed is $V_{\mathrm{gl}} + V_{\infty}$ and the minimum one is $V_{\mathrm{gl}} - V_{\infty}$); k_x is a gain that defines how aggressive the feedback action

Authorized licensed use limited to: TU Delft Library. Downloaded on January 20,2023 at 15:03:44 UTC from IEEE Xplore. Restrictions apply.

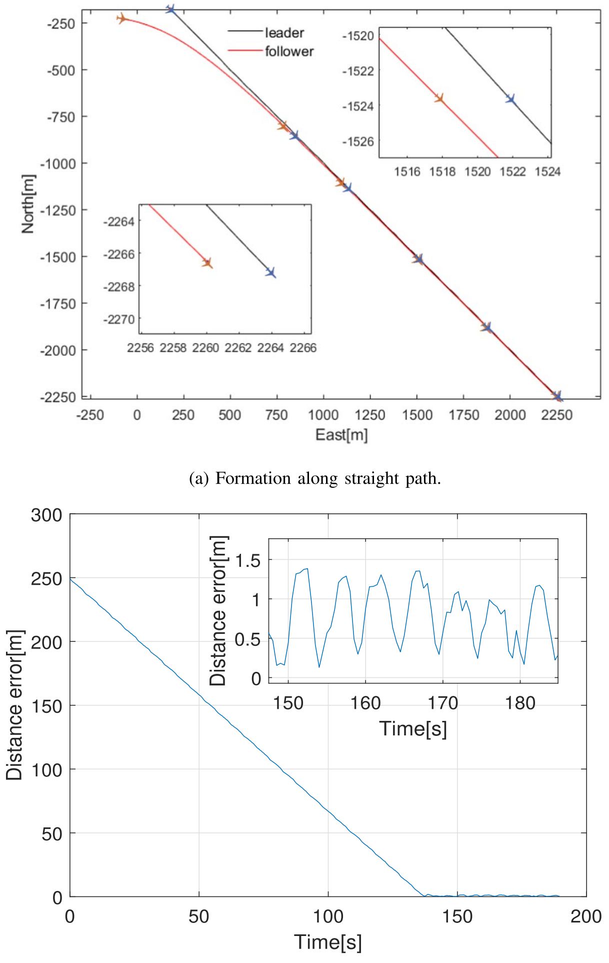

(a) Formation along straight path.

(b) Formation error, straight path.

Fig. 4. Proposed method: SITL experiment without wind, straight path.

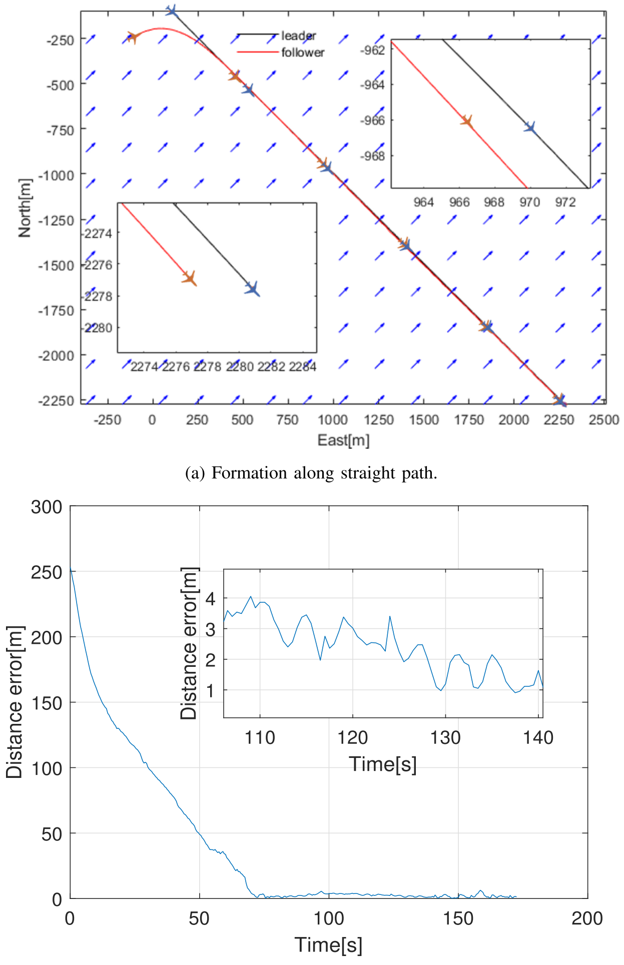

(a) Formation along straight path.

(b) Formation error, straight path.

Fig. 5. Proposed method: SITL experiment with wind, straight path.

is. The parameters in (16) have similar meanings as in the guidance law for a straight line in (4).

Remark 1: The proposed control law can be interpreted as a double vector field. One vector field is (16)*, which depends only on* y_E*: this has the structure of a standard vector field for a line that allows the follower to approach the line with the same course as the leader course and passing through the desired course point. The second vector field is for the velocity* (17) *and it depends only on* x_E*: it allows the follower to accelerate or decelerate in order to reach the desired point.*

A convenient way to visualize the proposed double vector field is to use a vector field similar to the straight-line vector field, but where the arrows of the vector field have different length: each arrow in the space that has a length proportional to the desired ground speed.

The guidance law for the follower solving the formation problem is

$$\chi_f^c = \chi_f + \frac{1}{\alpha}\dot{\chi}_f^d - \frac{\kappa}{\alpha}\mathrm{sat}\left(\frac{\tilde{\chi}_f}{\epsilon}\right) \tag{18}$$

$$V_{gf}^c = V_{gf} + \frac{1}{\beta}\dot{V}_{gf}^d + \frac{1}{\rho\beta}x_E - \frac{\kappa}{\beta}\mathrm{sat}\left(\frac{\tilde{V}_{gf}}{\epsilon}\right) \tag{19}$$

where the derivatives in (18), (19) can be calculated as

$$\dot{V}_{gf}^d = -V_\infty \frac{2}{\pi}\frac{k}{1+(k_x x_E)^2}\dot{x}_E \tag{20}$$

$$\dot{\chi}_f^d = -\chi_\infty \frac{2}{\pi}\frac{k}{1+(k_x d_f)^2}\dot{y}_E - \dot{\chi}_\infty \frac{2}{\pi}\tan^{-1}(k_y y_E) \tag{21}$$

and $\chi_\infty = \gamma_f - \pi - \chi_1$. The following theorem holds:

Theorem 1: The closed-loop system given by the leader (1)*, the follower* (8)*, the commands* (18)*,* (19) *with vector field* (16)*,* (17) *is asymptotically stable if*

$$\min\left(\frac{\rho\kappa}{V_{gf}}, \frac{\overline{y_E}}{2}\right) > \frac{\pi\epsilon\mu}{4\chi_\infty k} \tag{22}$$

where $\overline{y_E}$ *and* μ *are defined in the Appendix.*

Proof: See Appendix. □

The flowchart of the proposed algorithm is given in Figure 3. Communication between the leader and the follower is established to calculate the errors used by the controller. The formation vector field controlling the follower's velocity and course can be easily integrated with the velocity-hold loop and course-hold loop on top of the low-level controllers (attitude controllers). In other words, the proposed architecture is compatible with most open-source architectures such

Authorized licensed use limited to: TU Delft Library. Downloaded on January 20,2023 at 15:03:44 UTC from IEEE Xplore. Restrictions apply.

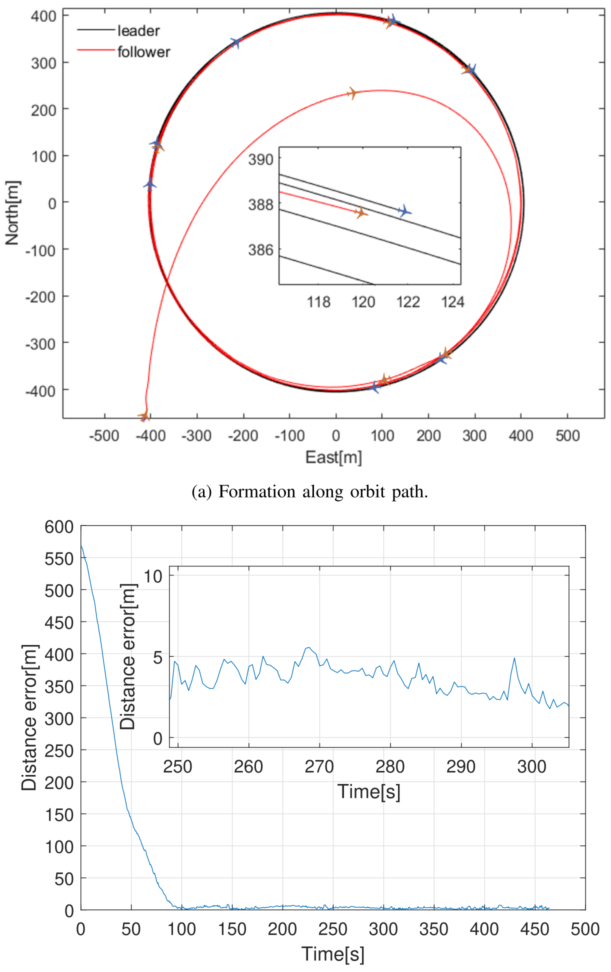

(a) Formation along orbit path.

(b) Formation error, orbit path.

Fig. 6. Proposed method: SITL experiment without wind, orbit path.

as ArduPilot, PX4, NAVIO2. The pseudo-code is shown in Algorithm 1: since the algorithm involves simple additions, multiplications, and static nonlinearities, its computational complexity is $\mathcal{O}(1)$.

IV. Validation

The algorithm is programmed in ROS and validated in software-in-the-loop (SITL) and hardware-in-the-loop (HITL) environments, using the PX4 autopilot suite. PX4 interacts with a companion PC (for SITL) or with Raspberry pi 3B+ (for HITL) by using the MAVROS communication package, while the 3D physical simulators of the UAV dynamics are Gazebo (for SITL) and X-plane (for HITL) [41]–[43]. The controllers run at 20Hz in SITL and 2Hz in HITL. The communication frequency between leader and followers is 2Hz in all tests. For comparison purposes, we adopt two methods:

- The state-of-the-art method proposed in [38] under the assumption of absence of wind. This method, abbreviated as "wind-absence method", assumes that the UAV air speed coincides with its ground speed, and that the UAV heading angle coincides with its course angle;
- The state-of-the-art method based on unicycle dynamics [44]. The method, abbreviated as "unicycle method" exploits the fact that the guidance dynamics for UAVs are analogous to the kinematic model of a unicycle mobile robot, cf. the survey [5].

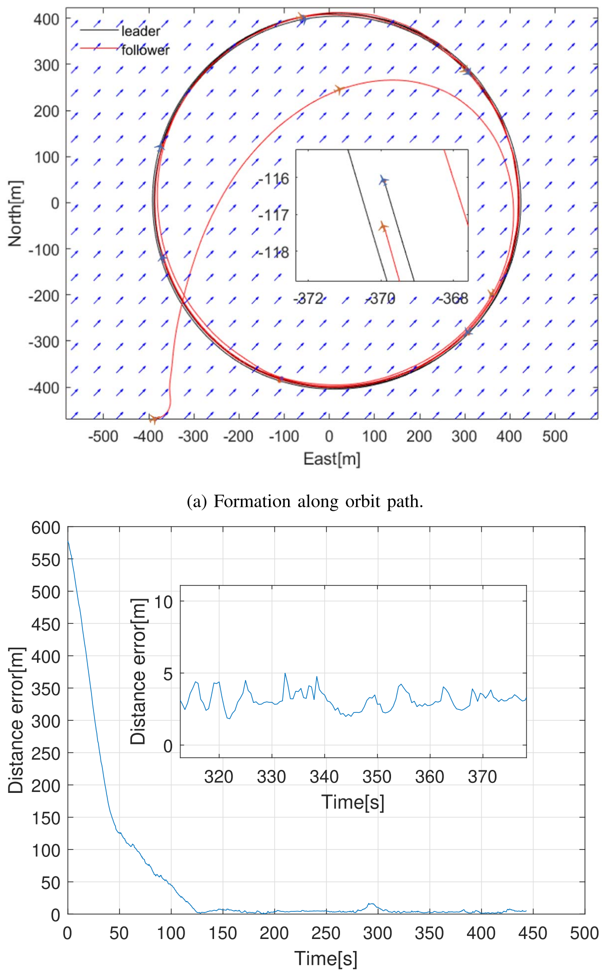

(a) Formation along orbit path.

(b) Formation error, orbit path.

Fig. 7. Proposed method: SITL experiment with wind, orbit path.

A. Software-In-The-Loop (SITL) Experiments

To assess the difference without and with wind, the wind plugin of Gazebo is used to create a wind scenario, using: WindForceMean = 2.5, WindForceMax = 3.5, WindGuestMean = 7, WindGuestMax = 10, WindDirectionMean = 45°.

1) Line and Orbit Paths: The experiments are first performed with two UAVs for a line and an orbit path (without and with wind). The desired gap between leader and follower is $(-2, -2)$m. In the straight path scenario, the leader flies at 18 m/s along a straight path, while the follower starts from a perpendicular position with respect to the path. In the orbit path scenario, the orbit has a radius of 400m. The follower starts from the bottom left region.

The results without wind are reported in Figures 4 and 5. The results in the presence of wind are reported in Figures 6 and 7. The formation errors below each path show that the presence of wind leads to larger errors. In particular, the wind makes the orbit scenario more challenging for two reasons:

Authorized licensed use limited to: TU Delft Library. Downloaded on January 20,2023 at 15:03:44 UTC from IEEE Xplore. Restrictions apply.

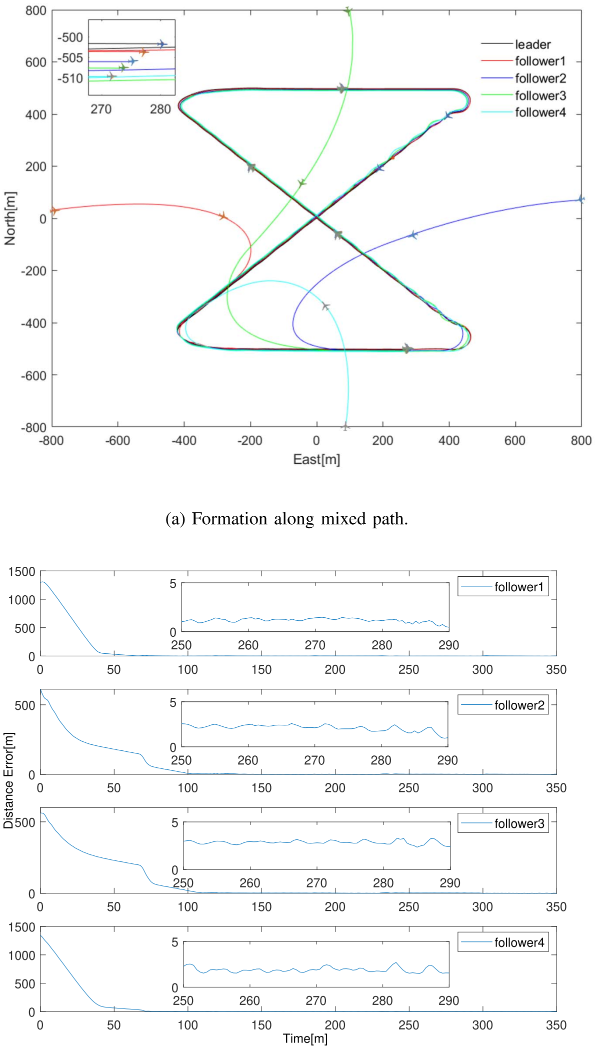

(a) Formation along mixed path.

(b) Formation error, mixed path.

Fig. 8. Proposed method: SITL experiment without wind, mixed path.

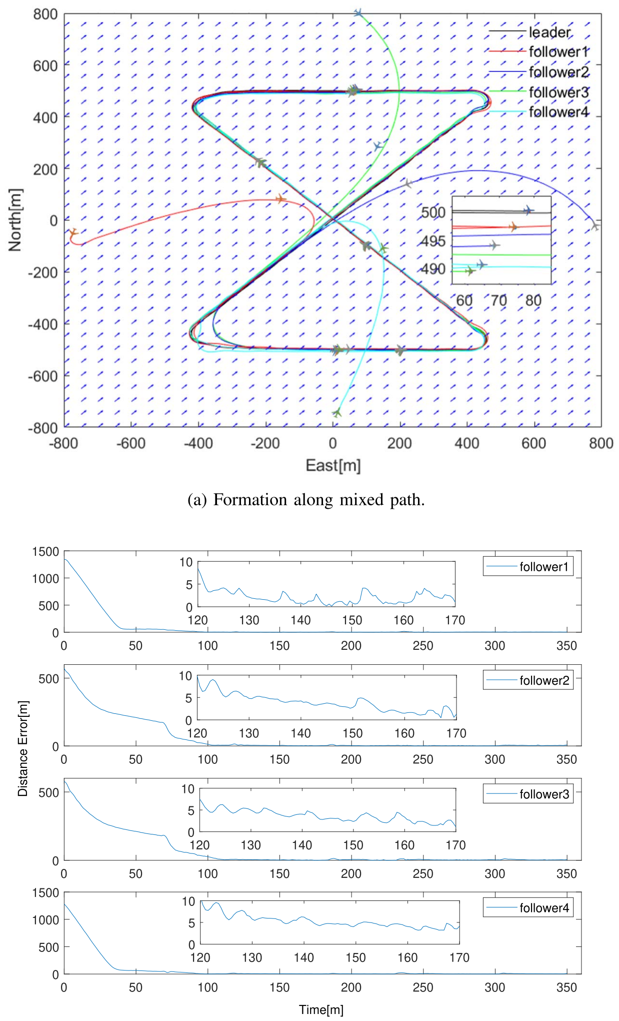

(a) Formation along mixed path.

(b) Formation error, mixed path.

Fig. 9. Proposed method: SITL experiment with wind, mixed path.

first, depending on the course, the wind affects the UAV with different intensity along the orbit; second, in order to keep the gap, the follower should perform an orbit of smaller radius and at smaller velocity which makes the flight harder.

2) Mixed Path: The mixed path is a combination of lines and orbits so that an 8-like shape is formed. We consider 1 leader with 4 followers, with desired gaps between leader and followers being $(-2, -2,)$, $(-4, -4)$, $(-6, -6)$, $(-8, -8)$ respectively. In order to evaluate the transient performance, we let the 4 followers start from different regions.

To conclude the SITL part, we report the results (in the presence of wind) of the wind-absence guidance [38] for a straight line (Figure 10), an orbit (Figure 11), and a mixed path (Figure 12), and of the unicycle guidance [44] for a straight line (Figure 13), an orbit (Figure 14) and a mixed path (Figure 15). Comparisons show that the proposed method performs more than 36% better than [38] and more than 120% better than [44] (see also Table II). The proposed method performs better than the wind-absence method because the wind-absence method cannot not properly handle the effect of the wind on UAV air speed and heading angle: the fact that these quantities are different from ground speed and course angle creates some bias in the formation error. The proposed method performs better than the unicycle method because with the unicycle method the follower UAV tries to imitate the course of the leader independently from its gap. On the other hand, with the proposed method, the follower UAV tries first to reduce the gap when the gap is large and then it will aim at aligning its course to the leader when the gap is smaller.

B. Hardware-In-The-Loop (HITL) Experiments

In the HITL environment, the code runs on PX4 hardware interfaced to the rest of the system as shown in Figure 16a. X-plane provides the fixed-wing dynamics, and connects with the Pixhawk board by a serial port. The proposed method runs in ROS in a Raspberry pi 3B+. The WiFi module in the Raspberry pi 3B+ is used for communication between the leader and the followers. The HITL setting allows to check the compatibility of the implementation with the true

Authorized licensed use limited to: TU Delft Library. Downloaded on January 20,2023 at 15:03:44 UTC from IEEE Xplore. Restrictions apply.

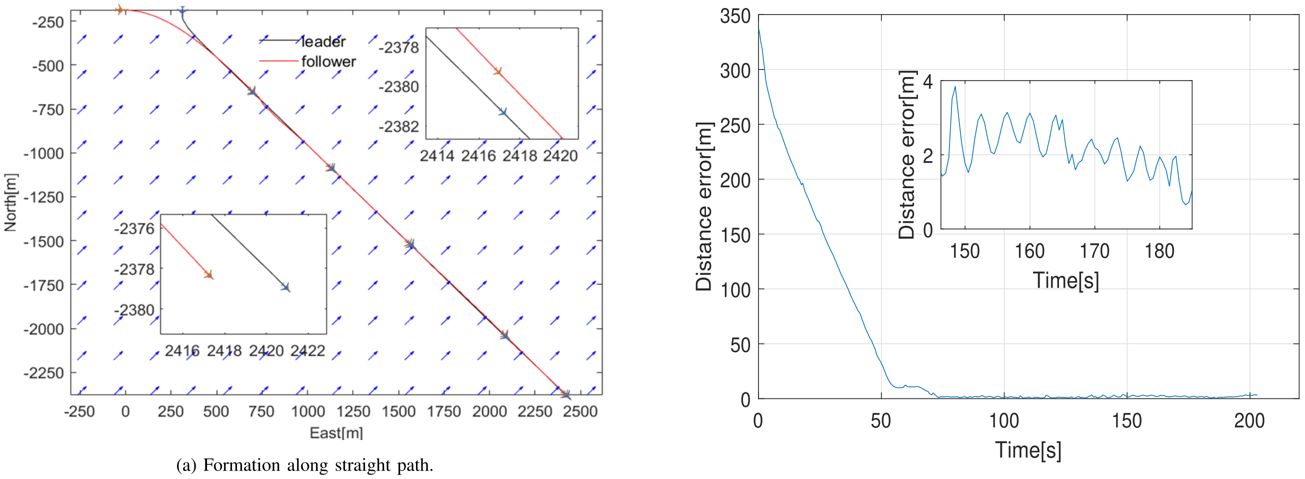

(a) Formation along straight path.

(b) Formation error, straight path.

Fig. 10. State-of-the-art method assuming absence of wind: experiments with wind, straight path.

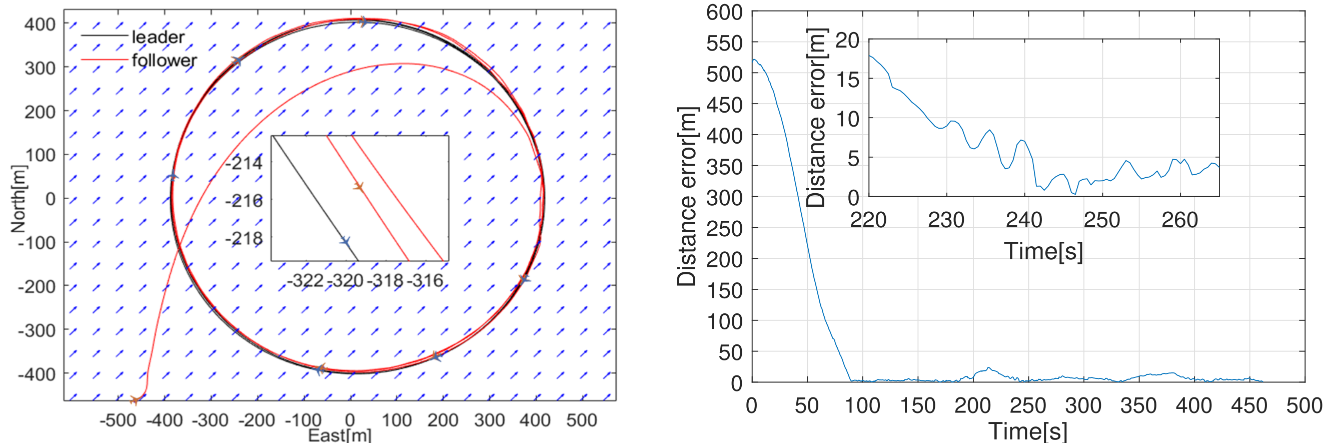

(a) Formation along orbit path.

(b) Formation error, orbit path.

Fig. 11. State-of-the-art method assuming absence of wind: experiments with wind, orbit path.

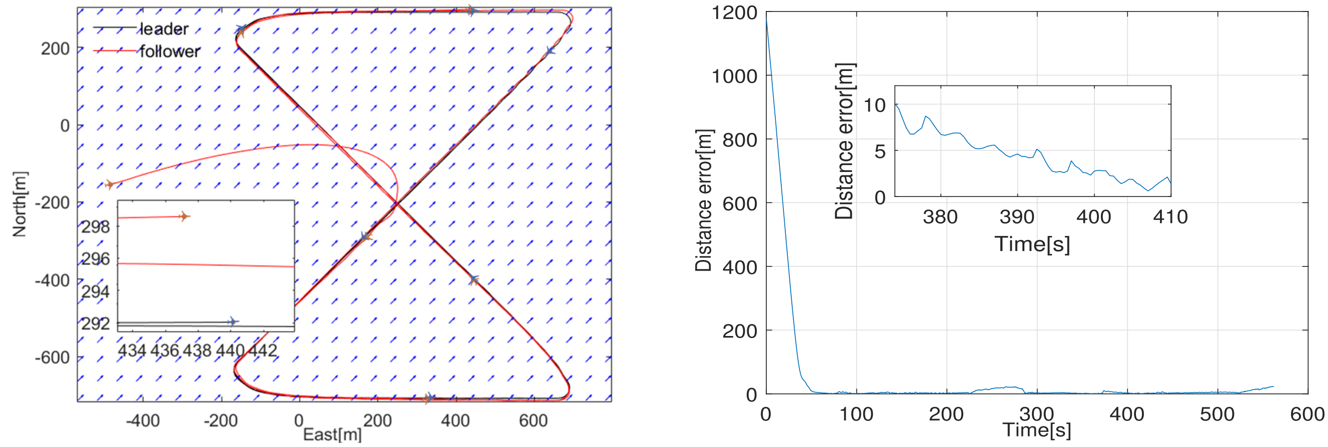

(a) Formation along mixed path.

(b) Formation error, mixed path.

Fig. 12. State-of-the-art method assuming absence of wind: experiments with wind, mixed path.

hardware. Most importantly, HITL allows to test the algorithm in the presence of realistic communication time delays and packet losses, which will inevitable influence the algorithm results. Because X-plane only supports 1 UAV for each PC, we tested 2 UAVs at same time as shown in Figure 16b.

Similarly to the SITL scenario, we test a straight line path, an orbit path and a mixed path, all of them in the presence of wind. The results for the straight line are in Figure 17; the results for the orbit are in Figure 18; the results for the mixed path are in Figure 19. All the results

Authorized licensed use limited to: TU Delft Library. Downloaded on January 20,2023 at 15:03:44 UTC from IEEE Xplore. Restrictions apply.

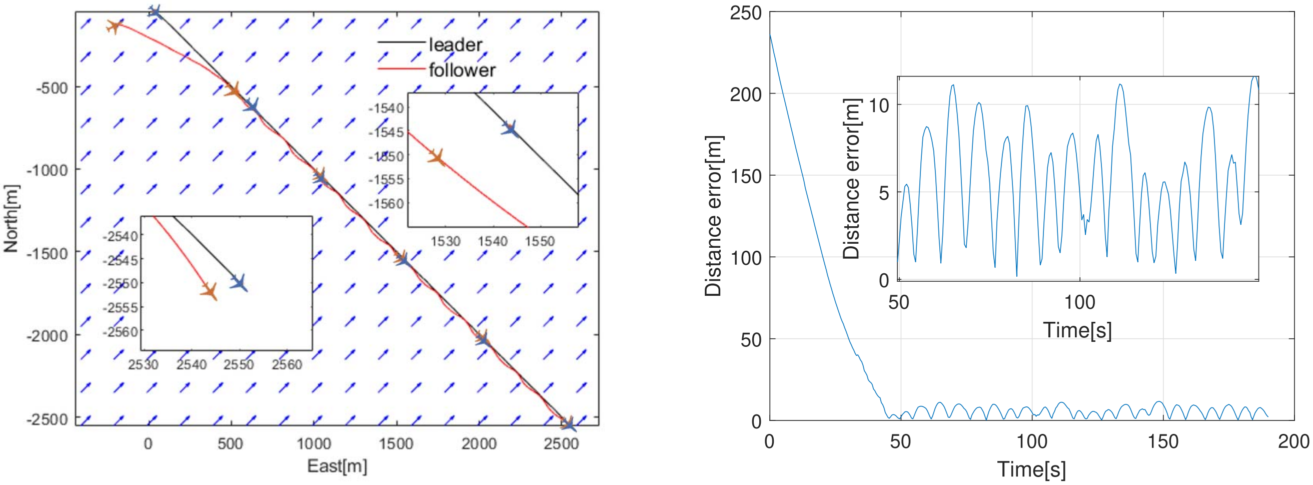

(a) Formation along straight path.

(b) Formation error, straight path.

Fig. 13. State-of-the-art method assuming unicycle dynamics: experiments with wind, straight path.

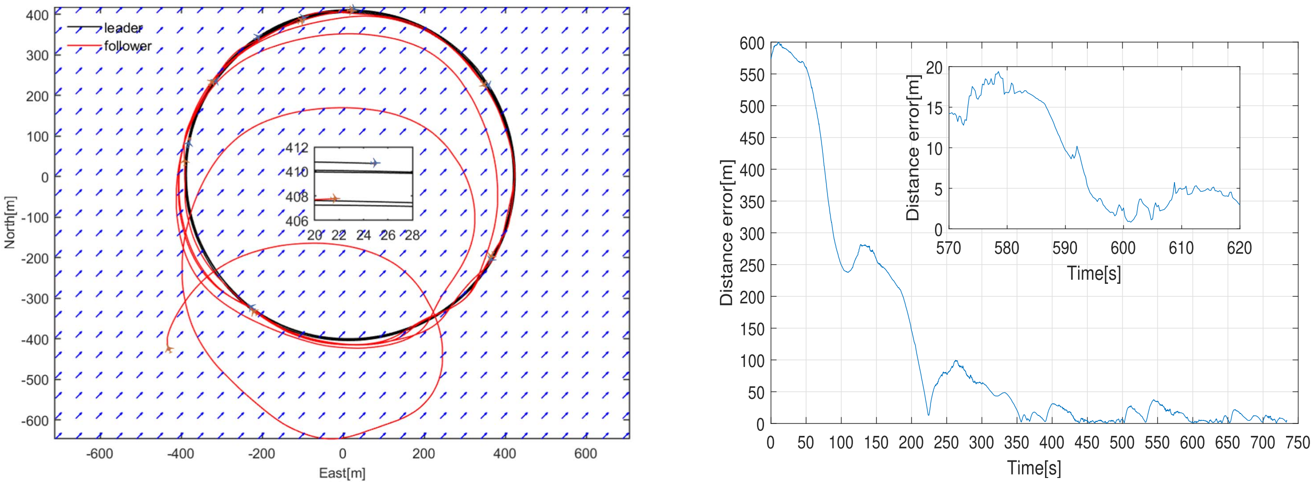

(a) Formation along orbit path.

(b) Formation error, orbit path

Fig. 14. State-of-the-art method assuming unicycle dynamics: SITL experiments with wind, orbit path.

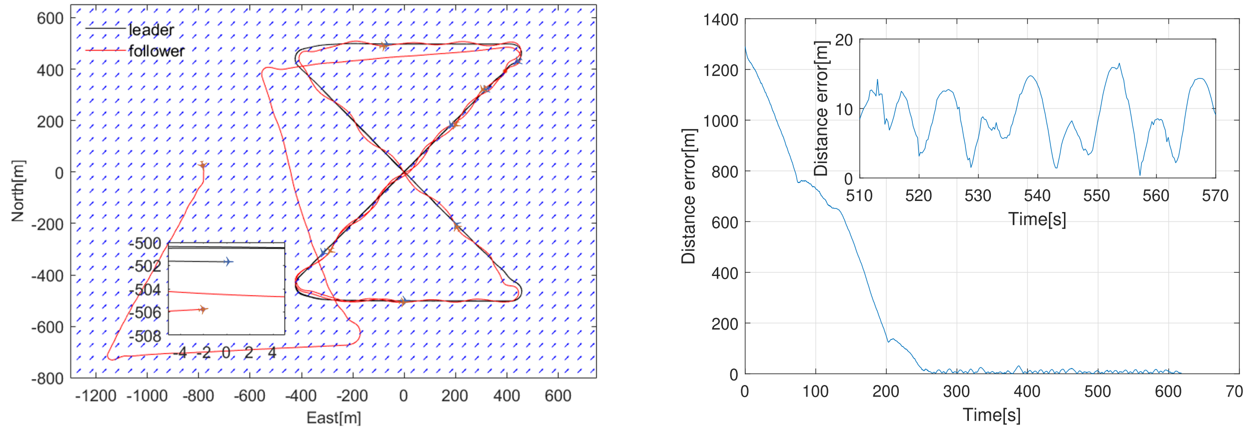

(a) Formation along mixed path.

(b) Formation error, mixed path.

Fig. 15. State-of-the-art method assuming unicycle dynamics: experiments with wind, mixed path.

are summarized in Table II: notice that all the results are steady-state formation errors, i.e. after removing the transient. The performance of the HITL degrades as compared to the corresponding SITL, which can be explained at least in two ways: first, the control frequency in HITL is 2Hz (in SITL it is 20Hz); second, time delays and packet losses become

Authorized licensed use limited to: TU Delft Library. Downloaded on January 20,2023 at 15:03:44 UTC from IEEE Xplore. Restrictions apply.

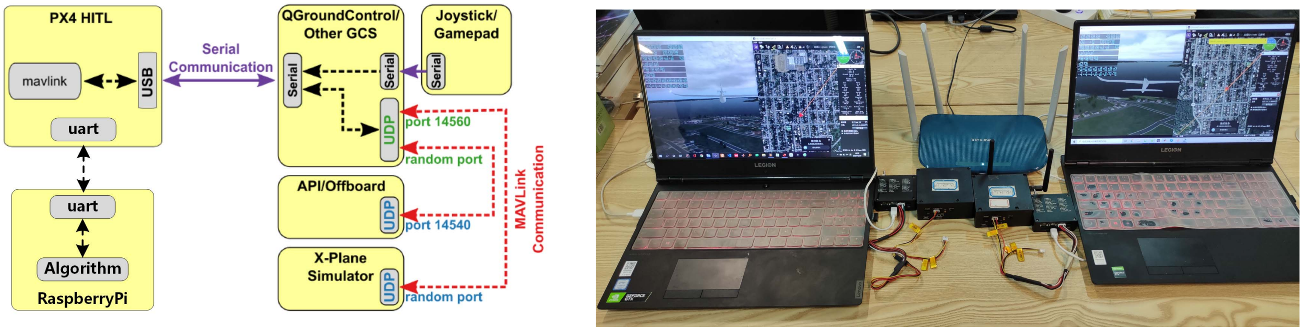

(a) Architecture of different modules.

(b) Hardware architecture.

Fig. 16. Setup for Hardware-In-The-Loop experiments, with PX4 as autopilot suite.

TABLE II

RMS Formation Error at Steady-State (After Convergence) Under Different Scenarios. In the Last Line, the Performance of Three Algorithms (Proposed, Absence, and Unicycle) in SITL With Wind Are Compared

	Line path RMS error	Orbit path RMS error	Mixed path RMS error
SITL: no wind (proposed)	0.826m	3.295m	1.804m, 1.906m, 2.132m, 2.168m
SITL: wind (proposed)	1.889m	5.228m	4.973m, 4.833m, 5.750m, 6.701m
HITL: wind (proposed)	5.468m	6.191m	7.782m
SITL: wind (absence)	2.562m **(+36%)**	8.411m **(+61%)**	7.884m **(+63%)**
SITL: wind (unicycle)	6.278m **(+232%)**	13.996m **(+168%)**	11.009m **(+121%)**

non-negligible in HITL. In fact, the USB, serial port, WiFi, and ROS node give a cumulative time delay which we have estimated to be between 20ms and 300ms. This is in line with results reported in the literature about ROS node operation [45], [46]. According to the leader air speed, these delays can result in 3-5m distance error [47], [48]. Therefore, the presented results provide a realistic validation of the proposed method. As a matter of fact, Table I shows that the errors of the proposed algorithm with HITL implementation are much smaller than the kinematic-based method with SITL implementation: this shows good performance even with high-latency communication.

V. Conclusion

This paper has proposed a vector field method to formation control of fixed-wing Unmanned Aerial Vehicles, by means of a non-uniform vector field (the field can change in both magnitude and direction). Stability of the proposed method was analyzed. Validations have been carried out in software-in-the-loop and hardware-in-the-loop comparative experiments using PX4 autopilot. It was shown that the proposed formation control law can work even with high-latency communication.

Future work goes along similar lines as the recent progress of the vector field method, e.g. tracking targets while achieving formation, handling more general curved paths, or tackling the inevitable uncertainty in the course dynamics.

Appendix

We consider the following candidate Lyapunov function:

$$W = \frac{1}{2}x_{\mathrm{E}}^2 + \frac{1}{2}\rho \tilde{V}_{\mathrm{gf}}^2 + \frac{1}{2}y_{\mathrm{E}}^2 + \frac{1}{2}\rho\tilde{\chi}_{\mathrm{f}}^2 \tag{23}$$

where $\tilde{V}_{\mathrm{gf}} = V_{\mathrm{gf}} - V_{\mathrm{gf}}^{\mathrm{d}}$ is the difference between the ground speed of the follower and its desired ground speed, while $\tilde{\chi}_{\mathrm{f}} = \chi_{\mathrm{f}} - \chi_{\mathrm{f}}^{\mathrm{d}}$ is the difference between the follower course and its desired course. In the following, we will analyze the proposed approach by splitting the Lyapunov function into two parts

$$W_y = \frac{1}{2}y_{\mathrm{E}}^2 + \frac{1}{2}\rho\tilde{\chi}_{\mathrm{f}}^2, \quad W_x = \frac{1}{2}x_{\mathrm{E}}^2 + \frac{1}{2}\rho\tilde{V}_{\mathrm{gf}}^2 \tag{24}$$

where the first part refers to lateral dynamics, and the second part refers to longitudinal dynamics. The stability analysis is done inside the boundary layer of the saturation function. The analysis outside the boundary layer, can be easily done along similar lines as [34].

A. Lateral Error and Course

We start by analyzing W_{y}: for this part, an approach similar to the analysis of the standard vector field can be adopted [34]. First, starting from (24), we calculate the time derivative

$$\begin{aligned} \dot{W}_y &= y_{\mathrm{E}}\dot{y}_{\mathrm{E}} + \rho\tilde{\chi}_{\mathrm{f}}\dot{\tilde{\chi}}_f \\ &= V_{\mathrm{gf}}y_{\mathrm{E}}\sin(\tilde{\chi}_{\mathrm{f}} + \chi_{\mathrm{f}}^{\mathrm{d}} - \chi_{\mathrm{l}}) - \rho\frac{k}{\epsilon}\tilde{\chi}_{\mathrm{f}}^2 \\ &\leq -\rho\frac{\kappa}{\epsilon}\tilde{\chi}_{\mathrm{f}}^2 + V_{\mathrm{gf}}y_{\mathrm{E}}\sin(\hat{\chi}_{\mathrm{f}}^{\mathrm{d}}) \\ &\quad + V_{\mathrm{gf}}y_{\mathrm{E}}\sin(\hat{\chi}_{\mathrm{f}}^{\mathrm{d}} + \tilde{\chi}_{\mathrm{f}}) - \sin(\hat{\chi}_{\mathrm{f}}^{\mathrm{d}}) \end{aligned} \tag{25}$$

where we have defined $\hat{\chi}_{\mathrm{f}}^{\mathrm{d}} = \chi_{\mathrm{f}}^{\mathrm{d}} - \chi_{\mathrm{l}}$ for compactness. The following inequalities hold

$$\begin{aligned} &|\sin(\hat{\chi}_{\mathrm{f}}^{\mathrm{d}} + \tilde{\chi}_{\mathrm{f}}) - \sin(\hat{\chi}_{\mathrm{f}}^{\mathrm{d}})| \\ &\quad = |\sin(\hat{\chi}_{\mathrm{f}}^{\mathrm{d}})\cos(\tilde{\chi}_{\mathrm{f}}) + \cos(\hat{\chi}_{\mathrm{f}}^{\mathrm{d}})\sin(\tilde{\chi}_{\mathrm{f}}) - \sin(\hat{\chi}_{\mathrm{f}}^{\mathrm{d}})| \\ &\quad = |\sin(\hat{\chi}_{\mathrm{f}}^{\mathrm{d}})(\cos(\tilde{\chi}_{\mathrm{f}}) - 1) + \cos(\hat{\chi}_{\mathrm{f}}^{\mathrm{d}})\sin(\tilde{\chi}_{\mathrm{f}})| \\ &\quad \leq |\cos(\tilde{\chi}_{\mathrm{f}} - 1) + \sin(\tilde{\chi}_{\mathrm{f}})| \leq 2|\tilde{\chi}_{\mathrm{f}}|. \end{aligned}$$

Authorized licensed use limited to: TU Delft Library. Downloaded on January 20,2023 at 15:03:44 UTC from IEEE Xplore. Restrictions apply.

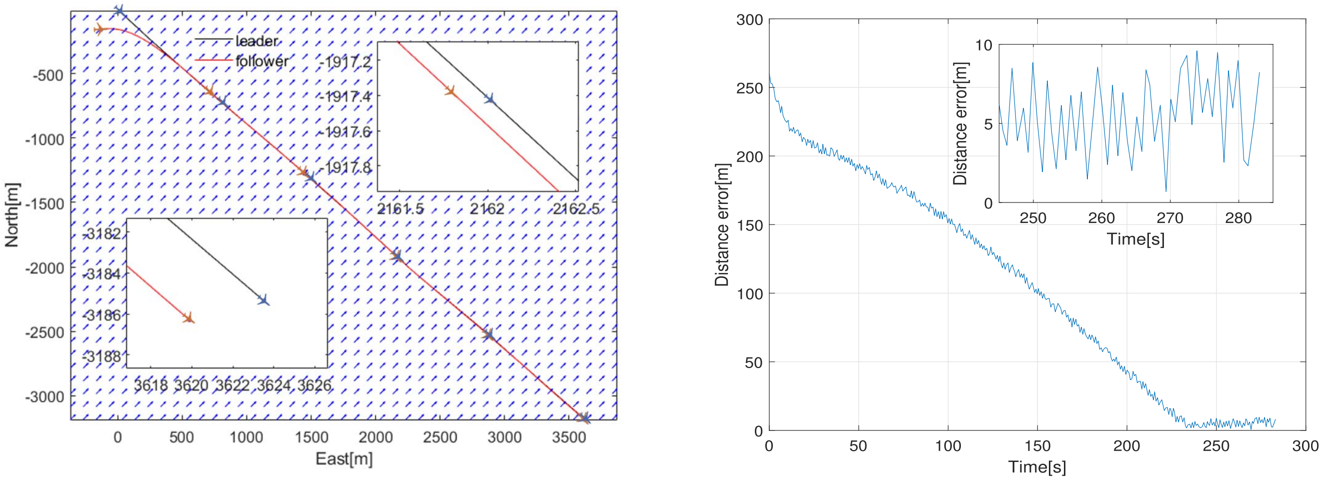

(a) Formation along straight path.

(b) Formation error, straight path.

Fig. 17. HITL experiment with wind, straight path.

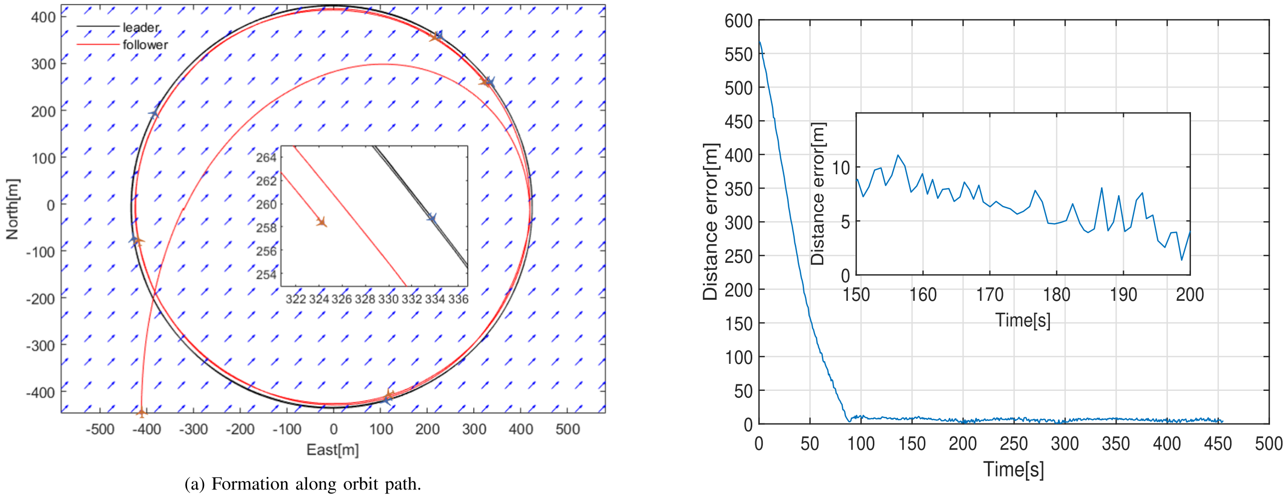

(a) Formation along orbit path.

(b) Formation error, orbit path.

Fig. 18. HITL experiment with wind, orbit path.

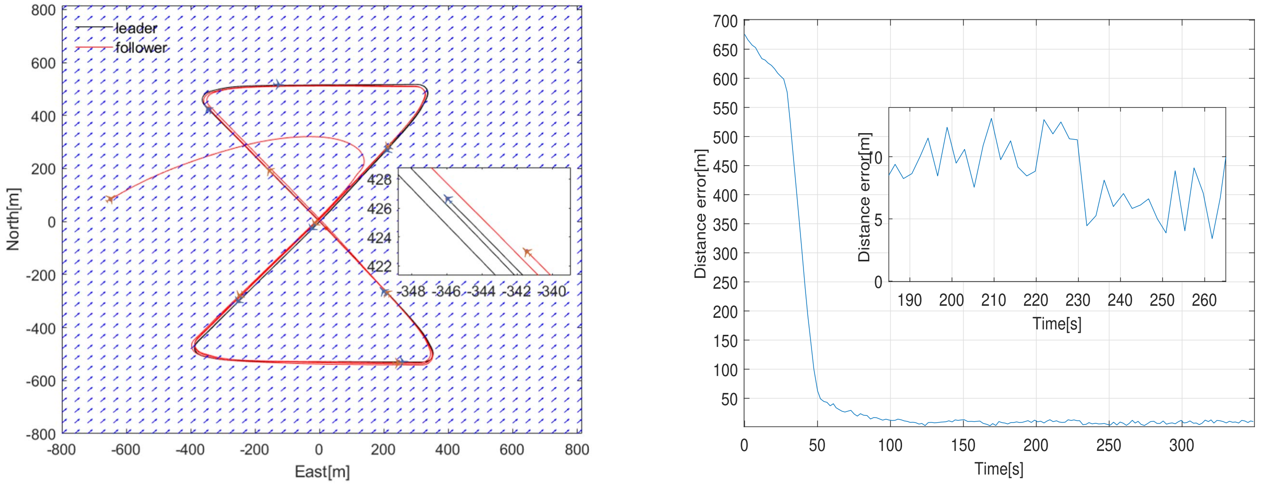

(a) Formation along mixed path.

(b) Formation error, mixed path.

Fig. 19. HITL experiment with wind, mixed path.

Authorized licensed use limited to: TU Delft Library. Downloaded on January 20,2023 at 15:03:44 UTC from IEEE Xplore. Restrictions apply.

The time derivative of W_y becomes

$$\begin{aligned}\dot{W}_y &\leq -\rho\frac{\kappa}{\epsilon}\tilde{\chi}_{\mathrm{f}}^2 + 2V_{\mathrm{gf}}|y_{\mathrm{E}}||\tilde{\chi}_{\mathrm{f}}| + V_{\mathrm{gf}}y_{\mathrm{E}}\sin(\chi_{\mathrm{f}}^{\mathrm{d}} - \chi_{\mathrm{l}})\\ &= -\rho\frac{\kappa}{\epsilon}\tilde{\chi}_{\mathrm{f}}^2 + 2V_{\mathrm{gf}}|y_{\mathrm{E}}||\tilde{\chi}_{\mathrm{f}}|\\ &\quad - V_{\mathrm{gf}}y_{\mathrm{E}}\sin(\chi_\infty\frac{2}{\pi}\tan^{-1}(ky_{\mathrm{E}}) - \frac{\pi}{2}). \qquad (26)\end{aligned}$$

In order to have $\dot{W}_y$ negative, we can distinguish two cases. The two cases are obtained by defining the function

$$\phi(y_{\mathrm{E}}) = y_{\mathrm{E}}\sin\left(\frac{2\chi_\infty}{\pi}\tan^{-1}(ky_{\mathrm{E}}) - \frac{\pi}{2}\right). \qquad (27)$$

We note that $\phi(y_{\mathrm{E}}) \to (2\chi_\infty k/\pi)y_{\mathrm{E}}^2$ for $ky_{\mathrm{E}} \to 0$ and $\phi(y_{\mathrm{E}}) \to (\sin\chi_\infty)y_{\mathrm{E}}$ for large value of ky_{E}. Consider a new function defined as:

$$\varphi(y_{\mathrm{E}}) = \begin{cases}\dfrac{2\chi_\infty k}{\mu\pi}y_{\mathrm{E}}^2, & \text{if } |y_{\mathrm{E}}| \leq \overline{y_{\mathrm{E}}}\\ \dfrac{2\chi_\infty k\overline{y_{\mathrm{E}}}}{\mu\pi}(2|y_{\mathrm{E}}| - \overline{y_{\mathrm{E}}}), & \text{otherwise.}\end{cases} \qquad (28)$$

Then we have to find μ such that $0 < \varphi(y_{\mathrm{E}}) \leq \phi(y_{\mathrm{E}})$. Since the functions are symmetric, we will restrict our attention to $y_{\mathrm{E}} \geq 0$ and aim to show that $\varphi(y_{\mathrm{E}}) \leq \phi(y_{\mathrm{E}})$. Given this reasoning, the following two cases are defined

- Case 1: $0 \leq y_{\mathrm{E}} \leq \overline{y_{\mathrm{E}}}$
- Case 2: $y_{\mathrm{E}} > \overline{y_{\mathrm{E}}}$

which are analyzed in the following.

Case 1: For $0 \leq y_{\mathrm{E}} \leq \overline{y_{\mathrm{E}}}$, we have

$$\begin{aligned}\phi'(y_{\mathrm{E}}) &= \sin\left(\frac{2\chi_\infty}{\pi}\tan^{-1}(ky_{\mathrm{E}}) - \frac{\pi}{2}\right)\\ &\quad + \frac{2k\chi_\infty}{\pi}y_{\mathrm{E}}\left[\frac{\cos(\frac{2\chi_\infty\tan^{-1}(ky_{\mathrm{E}})}{\pi})}{1+(ky_{\mathrm{E}})^2}\right]\\ &\geq \frac{4\chi_\infty k}{\pi}y_{\mathrm{E}}\left[\frac{1}{2}\frac{\cos(\frac{2\chi_\infty\tan^{-1}(ky_{\mathrm{E}})}{\pi})}{1+(ky_{\mathrm{E}})^2}\right]\\ &\geq \frac{4\chi_\infty k}{\pi}y_{\mathrm{E}}\left[\frac{1}{2}\frac{\cos(\frac{2\chi_\infty\tan^{-1}(k\overline{y_{\mathrm{E}}})}{\pi})}{1+(k\overline{y_{\mathrm{E}}})^2}\right]\\ &\geq \frac{4\chi_\infty k}{\pi}y_{\mathrm{E}} = \varphi'(y_{\mathrm{E}}) \qquad (29)\end{aligned}$$

so if we select μ such that

$$\mu \geq \frac{2(1+(k\overline{y_{\mathrm{E}}})^2)}{\cos\left(\frac{2\chi_\infty}{\pi}\tan^{-1}(k\overline{y_{\mathrm{E}}})\right)} \qquad (30)$$

then $\varphi'(y_{\mathrm{E}}) \leq \phi'(y_{\mathrm{E}})$.

Case 2: On the other side, for $y_{\mathrm{E}} > \overline{y_{\mathrm{E}}}$, we have

$$\begin{aligned}\phi(y_{\mathrm{E}}) &= y_{\mathrm{E}}\sin(\frac{2\chi_\infty}{\pi}\tan^{-1}(ky_{\mathrm{E}}))\\ &\geq y_{\mathrm{E}}\sin(\frac{2\chi_\infty}{\pi}\tan^{-1}(k\overline{y_{\mathrm{E}}})) \qquad (31)\end{aligned}$$

This implies that $\phi(y_{\mathrm{E}}) \geq \varphi(y_{\mathrm{E}})$ if:

$$\mu \geq \frac{4\chi_\infty k\overline{y_{\mathrm{E}}}}{\pi\sin(\frac{2\chi_\infty}{\pi}\tan^{-1}(k\overline{y_{\mathrm{E}}}))}. \qquad (32)$$

So we obtain that $\varphi(y_{\mathrm{E}}) \leq \phi(y_{\mathrm{E}})$ for both cases.

Case 1: For $|y_{\mathrm{E}}| \leq \overline{y_{\mathrm{E}}}$, the time derivative is

$$\dot{W}_y \leq -V_{\mathrm{gf}}\begin{pmatrix}|\tilde{\chi}_{\mathrm{f}}| & |y_{\mathrm{E}}|\end{pmatrix}\begin{pmatrix}\dfrac{\rho k}{\epsilon V_{\mathrm{gf}}} & -1\\ -1 & \dfrac{2\chi_\infty k}{\mu\pi}\end{pmatrix}\begin{pmatrix}|\tilde{\chi}|\\ |y_{\mathrm{E}}|\end{pmatrix} \qquad (33)$$

which is negative definite if the following holds:

$$\frac{\rho k\ 2\chi_\infty\kappa}{\epsilon V_{\mathrm{gf}}\mu\pi} > 1 \qquad (34)$$

Case 2: If $|y_{\mathrm{E}}| \geq \overline{y_{\mathrm{E}}}$, the fact that $\varphi(y_{\mathrm{E}}) \leq \phi(y_{\mathrm{E}})$ implies:

$$\dot{W}_y \leq -\frac{\rho\kappa}{\epsilon}\tilde{\chi}_{\mathrm{f}}^2 + 2\ V_{\mathrm{gf}}|y_{\mathrm{E}}||\tilde{\chi}_{\mathrm{f}}| - V_{\mathrm{gf}}\varphi(y_{\mathrm{E}}) \qquad (35)$$

which is negative definite i.e.

$$\dot{W}_y \leq 2\ V_{\mathrm{gf}}y_{\mathrm{E}}\left(\epsilon - \frac{\chi_\infty k\overline{y_{\mathrm{E}}}|y_{\mathrm{E}}|}{\mu\pi}\right) \qquad (36)$$

when the following inequality holds:

$$\frac{\chi_\infty k\overline{y_{\mathrm{E}}}}{\mu\epsilon\pi} > 1 \qquad (37)$$

The inequalities (34) and (37) (resulting in (22)) can both be satisfied with ϵ small enough, i.e. selecting the boundary layer small enough.

B. Longitudinal Error and Ground Speed

The rest of the analysis can be performed using y_{E}, $\tilde{\chi}_{\mathrm{f}} \to 0$ for the design described previously. Define the difference between the follower ground speed and the desired one:

$$\tilde{V}_{\mathrm{gf}} = V_{\mathrm{gf}} - V_{\mathrm{gf}}^{\mathrm{d}} = V_{\mathrm{gf}} - V_{\mathrm{gl}} - V_\infty\frac{2}{\pi}\tan^{-1}(kx_{\mathrm{E}}). \qquad (38)$$

This brings to the Lyapunov time derivative

$$\begin{aligned}\dot{W}_x &= x_{\mathrm{E}}\dot{x}_{\mathrm{E}} + \rho\tilde{V}_{\mathrm{gf}}\dot{\tilde{V}}_{\mathrm{gf}}\\ &= x_{\mathrm{E}}(V_{\mathrm{gf}}\sin(\chi_{\mathrm{f}} - \chi_{\mathrm{l}} - \frac{\pi}{2}) + V_{\mathrm{gl}}) + \rho\tilde{V}_{\mathrm{gf}}(\dot{V}_{\mathrm{gf}} - \dot{V}_{\mathrm{gf}}^{\mathrm{d}}).\end{aligned} \qquad (39)$$

Using the convergence property of $\tilde{\chi}_{\mathrm{f}}$, we obtain

$$\dot{W}_x = x_{\mathrm{E}}(V_{\mathrm{gl}} - V_{\mathrm{gf}} + \delta_x) + \rho\tilde{V}_{\mathrm{gf}}(\dot{V}_{\mathrm{gf}} - \dot{V}_{\mathrm{gf}}^{\mathrm{d}}) \qquad (40)$$

where $\delta_x = V_{\mathrm{gf}} + V_{\mathrm{gf}}\sin(\chi_{\mathrm{f}} - \chi_{\mathrm{l}} - \frac{\pi}{2}) \to 0$ thanks to convergence of $\tilde{\chi}_{\mathrm{f}}$, y_{E} and can be neglected. We continue the analysis of the time derivative by substituting the dynamics of V_{gf} in (8) and expressions of $V_{\mathrm{gf}}^{\mathrm{c}}$ in (19)

$$\begin{aligned}\dot{W}_x &= x_{\mathrm{E}}(V_{\mathrm{gl}} - V_{\mathrm{gf}}) + \rho\tilde{V}_{gf}(\beta(V_{\mathrm{gf}}^{\mathrm{c}} - V_{\mathrm{gf}}) - \tilde{V}_{\mathrm{gf}}^{\mathrm{d}})\\ &= x_{\mathrm{E}}(V_{\mathrm{gl}} - V_{\mathrm{gf}}) + \rho\tilde{V}_{gf}(\beta(\frac{1}{\rho\beta}x_{\mathrm{E}} - \frac{\kappa}{\beta\epsilon}\tilde{V}_{\mathrm{gf}}))\\ &= -x_{\mathrm{E}}\tilde{V}_{\mathrm{gf}} + x_{\mathrm{E}}(V_{\mathrm{gl}} - V_{\mathrm{gf}}^{\mathrm{d}}) + \rho\beta\frac{1}{\rho\beta}x_{\mathrm{E}} - \rho\frac{\kappa}{\epsilon}\tilde{V}_{\mathrm{gf}}^2\\ &= -V_\infty x_{\mathrm{E}}\frac{2}{\pi}\tan^{-1}(k_x x_{\mathrm{E}}) - \rho\frac{\kappa}{\epsilon}\tilde{V}_{\mathrm{gf}}^2. \qquad (41)\end{aligned}$$

By noticing that x_{E} and $\tan^{-1}(k_x x_{\mathrm{E}})$ are both functions in the 1st and 3rd quadrant, it is straightforward to conclude that the time derivative is negative definite, resulting in asymptotic stability. This concludes the analysis.

Authorized licensed use limited to: TU Delft Library. Downloaded on January 20,2023 at 15:03:44 UTC from IEEE Xplore. Restrictions apply.

Acknowledgment

Ximan Wang would like to thank Zobeer Mohammad for assistance on the kinematic algorithm and for a preliminary investigation of this topic during his M.Sc. degree at TU Delft.

References

[1] H. Huang, A. V. Savkin, and W. Ni, "Online UAV trajectory planning for covert video surveillance of mobile targets," *IEEE Trans. Autom. Sci. Eng.*, early access, Mar. 12, 2021, doi: 10.1109/TASE.2021.3062810.

[2] R. Rysdyk, "Unmanned aerial vehicle path following for target observation in wind," *J. Guid., Control, Dyn.*, vol. 29, no. 5, pp. 1092–1100, Sep. 2006.

[3] J. Keller, D. Thakur, M. Likhachev, J. Gallier, and V. Kumar, "Coordinated path planning for fixed-wing UAS conducting persistent surveillance missions," *IEEE Trans. Autom. Sci. Eng.*, vol. 14, no. 1, pp. 17–24, Jan. 2017.

[4] M. F. Bornebusch and T. A. Johansen, "Autonomous recovery of a fixed-wing UAV using a line suspended between two multirotor UAVs," *IEEE Trans. Aerosp. Electron. Syst.*, vol. 57, no. 1, pp. 90–104, Feb. 2021.

[5] P. B. Sujit, S. Saripalli, and J. B. Sousa, "Unmanned aerial vehicle path following: A survey and analysis of algorithms for fixed-wing unmanned aerial vehiclesss," *IEEE Control Syst.*, vol. 34, no. 1, pp. 42–59, Feb. 2014.

[6] A. Atyabi, S. M. Zadeh, and S. Nefti-Meziani, "Current advancements on autonomous mission planning and management systems: An AUV and UAV perspective," *Annu. Rev. Control*, vol. 46, pp. 196–215, Jan. 2020.

[7] T. Konrad, J.-J. Gehrt, J. Lin, R. Zweigel, and D. Abel, "Advanced state estimation for navigation of automated vehicles," *Annu. Rev. Control*, vol. 46, pp. 181–195, Feb. 2018.

[8] D. Sikeridis, E. E. Tsiropoulou, M. Devetsikiotis, and S. Papavassiliou, "Wireless powered public safety IoT: A UAV-assisted adaptive-learning approach towards energy efficiency," *J. Netw. Comput. Appl.*, vol. 123, pp. 69–79, Dec. 2018.

[9] P. A. Apostolopoulos, G. Fragkos, E. E. Tsiropoulou, and S. Papavassiliou, "Data offloading in uav-assisted multi-access edge computing systems under resource uncertainty," *IEEE Trans. Mobile Comput.*, early access, Mar. 31, 2021, doi: 10.1109/TMC.2021.3069911.

[10] D. R. Nelson, D. B. Barber, T. W. McLain, and R. W. Beard, "Vector field path following for small unmanned air vehicles," in *Proc. Amer. Control Conf.*, 2006, pp. 1–7.

[11] H. Chen, K. Chang, and C. S. Agate, "UAV path planning with tangent-plus-Lyapunov vector field guidance and obstacle avoidance," *IEEE Trans. Aerosp. Electron. Syst.*, vol. 49, no. 2, pp. 840–856, Apr. 2013.

[12] S. Zhao, X. Wang, Z. Lin, D. Zhang, and L. Shen, "Integrating vector field approach and input-to-state stability curved path following for unmanned aerial vehicles," *IEEE Trans. Syst., Man, Cybern. Syst.*, vol. 50, no. 8, pp. 2897–2904, Aug. 2020.

[13] S. Fari, X. Wang, S. Roy, and S. Baldi, "Addressing unmodeled path-following dynamics via adaptive vector field: A UAV test case," *IEEE Trans. Aerosp. Electron. Syst.*, vol. 56, no. 2, pp. 1613–1622, Apr. 2019.

[14] W. Yao, H. G. de Marina, B. Lin, and M. Cao, "Singularity-free guiding vector field for robot navigation," *IEEE Trans. Robot.*, vol. 37, no. 4, pp. 1206–1221, Aug. 2020.

[15] H. G. de Marina, Z. Sun, M. Bronz, and G. Hattenberger, "Circular formation control of fixed-wing UAVs with constant speeds," in *Proc. IEEE/RSJ Int. Conf. Intell. Robots Syst. (IROS)*, Sep. 2017, pp. 5298–5303.

[16] T. Z. Muslimov and R. A. Munasypov, "Consensus-based cooperative circular formation control strategy for multi-UAV system," in *Proc. Int. Russian Autom. Conf. (RusAutoCon)*, Sep. 2019, pp. 1–8.

[17] R. Singh and B. Bhushan, "Evolving intelligent system for trajectory tracking of unmanned aerial vehicles," *IEEE Trans. Autom. Sci. Eng.*, early access, Apr. 22, 2021, doi: 10.1109/TASE.2021.3072339.

[18] J. Wang and M. Xin, "Integrated optimal formation control of multiple unmanned aerial vehicles," *IEEE Trans. Control Syst. Technol.*, vol. 21, no. 5, pp. 1731–1744, Sep. 2013.

[19] W. Lin, "Distributed UAV formation control using differential game approach," *Aerosp. Sci. Technol.*, vol. 35, no. 1, pp. 54–62, 2014.

[20] O. Thakoor, J. Garg, and R. Nagi, "Multiagent UAV routing: A game theory analysis with tight price of anarchy bounds," *IEEE Trans. Automat. Sci. Eng.*, vol. 17, no. 1, pp. 100–116, Jan. 2020.

[21] Y. Liu, J. M. Montenbruck, D. Zelazo, M. Odelga, S. Rajappa, H. H. Bülthoff, F. Allgöwer, and A. Zell, "A distributed control approach to formation balancing and maneuvering of multiple multirotor UAVs," *IEEE Trans. Robot.*, vol. 34, no. 4, pp. 870–882, Aug. 2018.

[22] J. Zhang, J. Yan, and P. Zhang, "Multi-UAV formation control based on a novel back-stepping approach," *IEEE Trans. Veh. Technol.*, vol. 69, no. 3, pp. 2437–2448, Mar. 2020.

[23] Z. Zhen, G. Tao, Y. Xu, and G. Song, "Multivariable adaptive control based consensus flight control system for UAVs formation," *Aerosp. Sci. Technol.*, vol. 93, Oct. 2019, Art. no. 105336.

[24] D. Yue, S. Baldi, J. Cao, Q. Li, and B. De Schutter, "A directed spanning tree adaptive control solution to time-varying formations," *IEEE Trans. Control Netw. Syst.*, vol. 8, no. 2, pp. 690–701, Jun. 2021.

[25] Y. Zou and Z. Meng, "Coordinated trajectory tracking of multiple vertical take-off and landing UAVs," *Automatica*, vol. 99, pp. 33–40, Sep. 2019.

[26] J. Wang, Z. Zhou, C. Wang, and Z. Ding, "Cascade structure predictive observer design for consensus control with applications to UAVs formation flying," *Automatica*, vol. 121, Nov. 2020, Art. no. 109200.

[27] D. R. Nelson, D. B. Barber, T. W. McLain, and R. W. Beard, "Vector field path following for miniature air vehicles," *IEEE Trans. Robot.*, vol. 23, no. 3, pp. 519–529, Jun. 2007.

[28] X. Dong, B. Yu, Z. Shi, and Y. Zhong, "Time-varying formation control for unmanned aerial vehicles: Theories and applications," *IEEE Trans. Control Syst. Technol.*, vol. 23, no. 1, pp. 340–348, Jan. 2015.

[29] Y. Zou, Z. Zhou, Z. Meng, and X. Dong, "Distributed formation control for multiple vertical takeoff and landing UAVs with switching topologies," *IEEE/ASME Trans. Mechatronics*, vol. 23, no. 4, pp. 1750–1761, Aug. 2018.

[30] J. Wang, L. Han, X. Dong, Q. Li, and Z. Ren, "Distributed sliding mode control for time-varying formation tracking of multi-UAV system with a dynamic leader," *Aerosp. Sci. Technol.*, vol. 111, Apr. 2021, Art. no. 106549.

[31] X. Dong, Y. Hua, Y. Zhou, Z. Ren, and Y. Zhong, "Theory and experiment on formation-containment control of multiple multirotor unmanned aerial vehicle systems," *IEEE Trans. Autom. Sci. Eng.*, vol. 16, no. 1, pp. 229–240, Jan. 2019.

[32] S. Rathinam, R. Sengupta, and S. Darbha, "A resource allocation algorithm for multivehicle systems with nonholonomic constraints," *IEEE Trans. Autom. Sci. Eng.*, vol. 4, no. 1, pp. 98–104, Jan. 2007.

[33] J. Zhang, J. Yan, and P. Zhang, "Fixed-wing UAV formation control design with collision avoidance based on an improved artificial potential field," *IEEE Access*, vol. 6, pp. 78342–78351, 2018.

[34] R. W. Beard and T. W. McLain, *Small Unmanned Aircraft: Theory Practice*. Princeton, NJ, USA: Princeton Univ. Press, 2012.

[35] F. Liao, R. Teo, J. L. Wang, X. Dong, F. Lin, and K. Peng, "Distributed formation and reconfiguration control of VTOL UAVs," *IEEE Trans. Control Syst. Technol.*, vol. 25, no. 1, pp. 270–277, Apr. 2016.

[36] Y. Wang, M. Shan, and D. Wang, "Motion capability analysis for multiple fixed-wing UAV formations with speed and heading rate constraints," *IEEE Trans. Control Netw. Syst.*, vol. 7, no. 2, pp. 977–989, Jun. 2020.

[37] T. Z. Muslimov and R. A. Munasypov, "Adaptive decentralized flocking control of multi-UAV circular formations based on vector fields and backstepping," *ISA Trans.*, vol. 107, pp. 143–159, 2020.

[38] T. Z. Muslimov and R. A. Munasypov, "Consensus-based cooperative control of parallel fixed-wing UAV formations via adaptive backstepping," *Aerosp. Sci. Technol.*, vol. 109, Feb. 2021, Art. no. 106416.

[39] J.-S. Gutmann, E. Eade, P. Fong, and M. E. Munich, "Vector field SLAM—Localization by learning the spatial variation of continuous signals," *IEEE Trans. Robot.*, vol. 28, no. 3, pp. 650–667, Jun. 2012.

[40] J.-W. Kwon and D. Chwa, "Hierarchical formation control based on a vector field method for wheeled mobile robots," *IEEE Trans. Robot.*, vol. 28, no. 6, pp. 1335–1345, Dec. 2012.

[41] PX4. *Gazebo Simulation*. Accessed: Feb. 2021. [Online]. Available: https://docs.px4.io/master/en/simulation/gazebo.html

[42] *PX4-SITLgazebo*. Accessed: Feb. 2021. [Online]. Available: https://github.com/PX4/PX4-SITL_gazebo/blob/e580bbcd1eb6902c658ed3ece3b3b28dfd57eb17/models/plane/plane.sdf.jinja

[43] Gazebo. *Gazebo: Tutorials*. Accessed: Feb. 2021. [Online]. Available: http://gazebosim.org/tutorials

[44] D. Kostić, S. Adinandra, J. Caarls, N. van de Wouw, and H. Nijmeijer, "Collision-free tracking control of unicycle mobile robots," in *Proc. IEEE Conf. Decis. Control (CDC)*, May 2009, pp. 5667–5672.

[45] D. Tardioli, R. Parasuraman, and P. Ögren, "Pound: A ROS node for reducing delay and jitter in wireless multi-robot networks," 2017, *arXiv:1707.07540*.

Authorized licensed use limited to: TU Delft Library. Downloaded on January 20,2023 at 15:03:44 UTC from IEEE Xplore. Restrictions apply.

[46] R. Bottura, D. Babazadeh, K. Zhu, A. Borghetti, L. Nordström, and C. A. Nucci, "SITL and HLA co-simulation platforms: Tools for analysis of the integrated ICT and electric power system," in *Proc. Eurocon*, 2013, pp. 918–925.

[47] J. N. Gross, Y. Gu, and M. B. Rhudy, "Robust UAV relative navigation with DGPS, INS, and peer-to-peer radio ranging," *IEEE Trans. Autom. Sci. Eng.*, vol. 12, no. 3, pp. 935–944, Jul. 2015.

[48] L. Fusini, T. I. Fossen, and T. A. Johansen, "Nonlinear observers for GNSS- and camera-aided inertial navigation of a fixed-wing UAV," *IEEE Trans. Control Syst. Technol.*, vol. 26, no. 5, pp. 1884–1891, Sep. 2018.

Ximan Wang received the B.Sc. degree in software engineering from the Taiyuan University of Technology, China, in 2014, and the M.Sc. degree in automotive control system engineering from The University of Sheffield in 2016. He is currently pursuing the Ph.D. degree with the Delft Center for Systems and Control, Delft University of Technology. He was a Senior Engineer at the Systems Engineering Research Institute, Beijing, China. His research interests include UAV vector field control and UAV adaptive control.

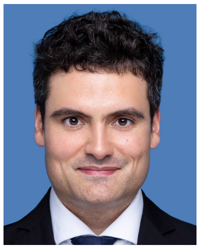

Simone Baldi (Senior Member, IEEE) received the B.Sc. degree in electrical engineering and the M.Sc. and Ph.D. degrees in automatic control engineering from the University of Florence, Italy, in 2005, 2007, and 2011, respectively. He is currently a Professor with the School of Mathematics and the School of Cyber Science and Engineering, Southeast University, with guest position at the Delft Center for Systems and Control, TU Delft, where he was an Assistant Professor. His research interests include adaptive and learning systems with applications in unmanned vehicles and smart energy systems. He was awarded Outstanding Reviewer of *Applied Energy* (2016) and *Automatica* (2017). He is a Subject Editor of *International Journal of Adaptive Control and Signal Processing*.

Xuewei Feng received the B.Sc. degree in software engineering from the Taiyuan University of Technology, China, in 2019, where he is currently pursuing the M.Sc. degree in software engineering. His research interests include UAV navigation and autonomous landing.

Changwei Wu received the B.Sc. degree in geographic information science from the China University of Geosciences, Wuhan, China, in 2017. He is currently pursuing the M.Sc. degree in software engineering with the Taiyuan University of Technology, China. His research interests include multi-agent systems and UAV navigation.

Hongwei Xie received the B.S. degree in computer engineering from the Dalian University of Technology, Dalian, China, in 1984, and the M.Sc. degree in computer science and the Ph.D. degree in electronic circuits and systems from the Taiyuan University of Technology, Taiyuan, China, in 1989 and 2008, respectively. She went to Auckland University as a Visiting Scholar in 2009 and Ottawa University as a Senior Visiting Scholar in 2016. She is currently a Professor with the Taiyuan University of Technology. Her research interests include artificial intelligence, intelligent software engineering, and high performance computing. She is a member of China Computer Federation and CCF High Performance Computing Committee and a Senior Member of Shanxi Computer Federation.

Bart De Schutter (Fellow, IEEE) received the Ph.D. degree *(summa cum laude)* in applied sciences from Katholieke Universiteit (KU), Leuven, Belgium, in 1996.

He is currently a Full Professor and the Department Head of the Delft Center for Systems and Control, Delft University of Technology, Delft, The Netherlands. He is the author or coauthor of three books, titled *Optimal Trajectory Planning and Train Scheduling for Urban Rail Transit Systems* (Springer, 2016), *Reinforcement Learning and Dynamic Programming Using Function Approximators* (CRC Press, 2010), and *Stability Analysis and Nonlinear Observer Design Using Takagi-Sugeno Fuzzy Models* (Springer, 2010), and more than 200 articles in international journals.

Prof. De Schutter was an Associate Editor of *Automatica* from 2004 to 2016. He is currently an Associate Editor of the IEEE TRANSACTIONS ON AUTOMATIC CONTROL and a Senior Editor of the IEEE TRANSACTIONS ON INTELLIGENT TRANSPORTATION SYSTEMS.

Authorized licensed use limited to: TU Delft Library. Downloaded on January 20,2023 at 15:03:44 UTC from IEEE Xplore. Restrictions apply.